PARTICLE CRACKING DAMAGE EVOLUTION IN 7075 WROUGHT ALUMINUM ALLOY UNDER MONOTONIC AND CYCLIC LOADING CONDITIONS

A Thesis
Presented to
The Academic Faculty

by

Joel Harris

In Partial Fulfillment
of the Requirements for the Degree
Master of Science in the
School of Materials Science and Engineering

Georgia Institute of Technology
December, 2005

PARTICLE CRACKING DAMAGE EVOLUTION IN 7075 WROUGHT ALUMINUM ALLOY UNDER MONOTONIC AND CYCLIC LOADING CONDITIONS

Approved by:

Dr. Arun M. Gokhale, Advisor
School of Materials Science and Engineering
Georgia Institute of Technology

Dr. Ken Gall
School of Materials Science and Engineering
Georgia Institute of Technology

Dr. Naresh Thadhani
School of Materials Science and Engineering
Georgia Institute of Technology

Date Approved: 11/22/05

ACKNOWLEDGEMENTS

I would like to thank many individuals who have contributed to my completion of this document. First and foremost, I would like to thank my advisor Dr. Arun Gokhale for his guidance, support, and encouragement throughout my time as a student at the Georgia Institute of Technology. Without his constant guidance, this work would not be possible.

Furthermore, I would like to thank my thesis committee members Dr. Arun Gokhale, Dr. Ken Gall, and Dr. Naresh Thadhani for their time, effort, and suggestions from reading and reviewing my thesis work. I would like to thank Gautam Patel for his input and training with sample preparation methods. I would also like to thank my colleagues Arun Sreeranganathan, Yuxiong Mao, Soon Gi Lee, Harpreet Singh, and Scott Lieberman for their support. I would like to thank the people at Northrupp Grumman and those involved from Mississippi State University for providing samples and mechanical testing. I would also like to express my gratitude to Dr. Mark Horstemeyer for his encouragement and recommendation in my pursuit of this degree.

In addition, I would like to especially thank my mother, father, brother, and wife, without whose support I would not be where I am today.

The funding for this project was provided by the US National Science Foundation (grant no. DMR-0404668) and the PROGNOSIS program of DARPA. The financial support is gratefully acknowledged. I would like to thank Boeing for their financial support of my graduate studies and work through a Graduate Fellowship.

TABLE OF CONTENTS

LIST OF TABLES

LIST OF FIGURES

SUMMARY

Plastic deformation and fracture of numerous wrought Al-alloys involves cracking of the coarse constituent particles, and therefore it is of interest to quantitatively characterize them. To the best of author's knowledge, detailed *quantitative* microstructural data on the cracking of coarse constituent particles in 7xxx series wrought Al-alloys have not been reported in the literature to date. In this study particle cracking is quantitatively characterized as a function of monotonic and cyclic loading conditions in an Al-Zn-Mg-Cu-base wrought Al-alloy. Numerous microstructural descriptors such as size distributions, orientation distributions, two-point correlation functions, nearest neighbor distributions, volume fractions, and number densities are experimentally measured for both overall Fe-rich particle population as well as cracked Fe-rich particles using stereological and digital image analysis techniques. A novel digital image analysis approach is developed and used for the automatic and efficient segmentation of cracked particles due to monotonic loading. However, difficulties in detecting fatigue cracks result in manual measurements which are very tedious and time consuming.

The data suggests useful relationships for damage modeling such as: (1) a linear relationship between particle cracking and strain exists for the monotonic loading condition, (2) for all loading conditions studied, the larger particles crack preferentially, (3) a complete set of nearest neighbor distributions can be generated with measurements of a single cracked nearest neighbor distribution if the number densities of cracked particles are known for each applied strain Nonetheless, more studies are needed on

characterization of particle cracking under cyclic loading conditions to better understand the damage nucleation processes due to particle cracking.

CHAPTER I

INTRODUCTION, PROBLEM FORMULATION, AND OBJECTIVES

7xxx series Al-Zn-Mg-Cu-base wrought Al-alloy products are widely used for aerospace structural applications where monotonic and cyclic mechanical properties are of prime concern [1]. Microstructure of these commercial alloys usually contains brittle coarse constituent particles or inclusions of Fe-rich intermetallic compounds and Mg_2Si, typically in the size range of 1 to 50 μm [2,3]. Figure 1 shows the microstructure of a hot-rolled 7075 Al-alloy (an important alloy of 7xxx series) depicting the coarse constituent particles. In this microstructure, the dark equiaxed particles are Mg_2Si particles, where as the gray particles are the Fe-rich intermetallic constituent particles. Observe that the Fe-rich constituent particles have complex shapes/morphologies; they are spatially non-uniform (clustered); and have partially anisotropic morphological orientations. Plastic deformation and fracture of 7xxx series alloys (as well as of numerous other wrought Al-alloys) is associated with gradual microstructural damage accumulation that involves cracking of the coarse constituent particles, growth of voids around the cracked particles, and the void coalescence [4-8]. Figure 2 shows cracked Fe-rich constituent particles in a hot-rolled 7075 Al-alloy and growth of voids around the cracked particles. To understand and model the microstructural damage evolution

processes such as particle cracking, quantitative microstructural data associated with the damage features are required under monotonic as well as cyclic loading conditions. Such data also form an important input for development of the internal state variables (ISV) based models [9-11] for prediction of damage evolution and fracture in 7xxx series Al-alloys under complex multi-axial monotonic and cyclic loading conditions. An important component of the microstructural damage evolution in the 7xxx series Al-alloys is the damage nucleation due to cracking of the coarse constituent particles. Accordingly, quantitative characterization of cracking of the coarse constituent particles as a function of strain under monotonic loading conditions and as a function of the number of cycles under cyclic loading conditions is of interest.

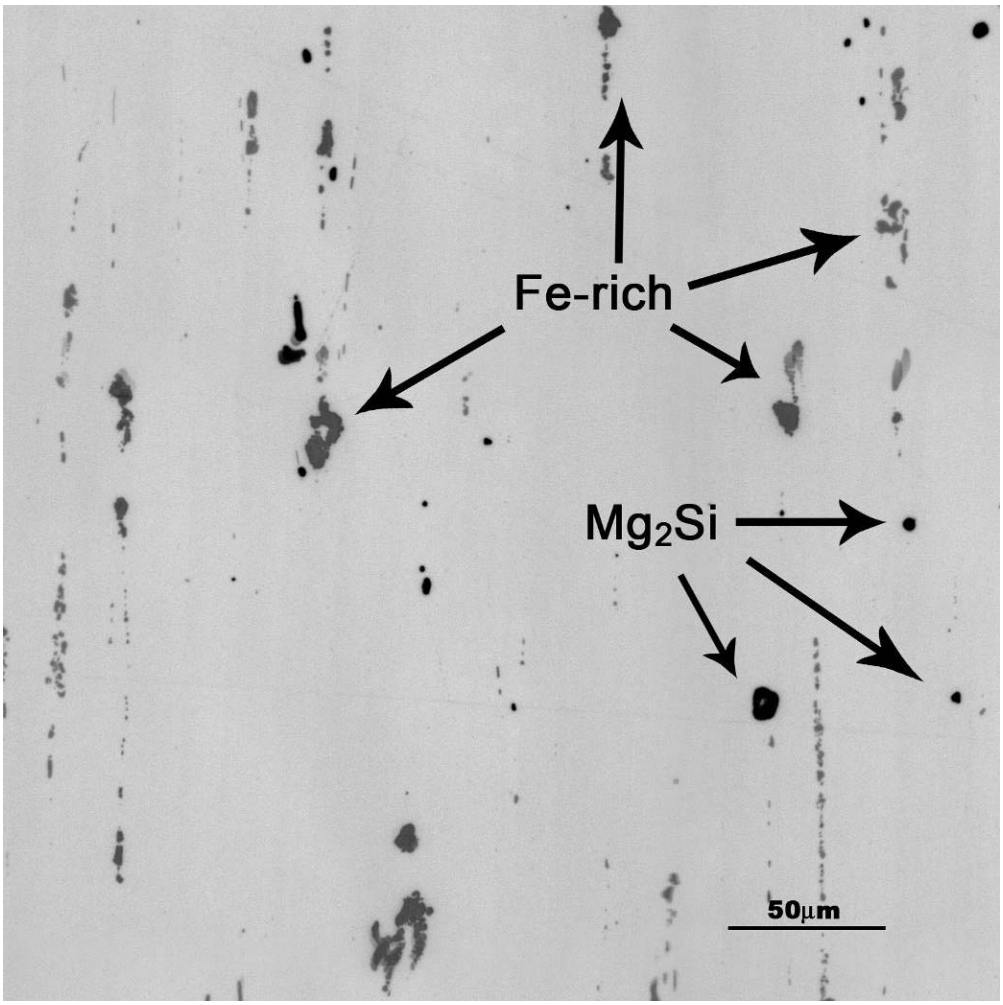

Figure 1 Microstructure of a Hot Rolled 7075 T651 Al-alloy.

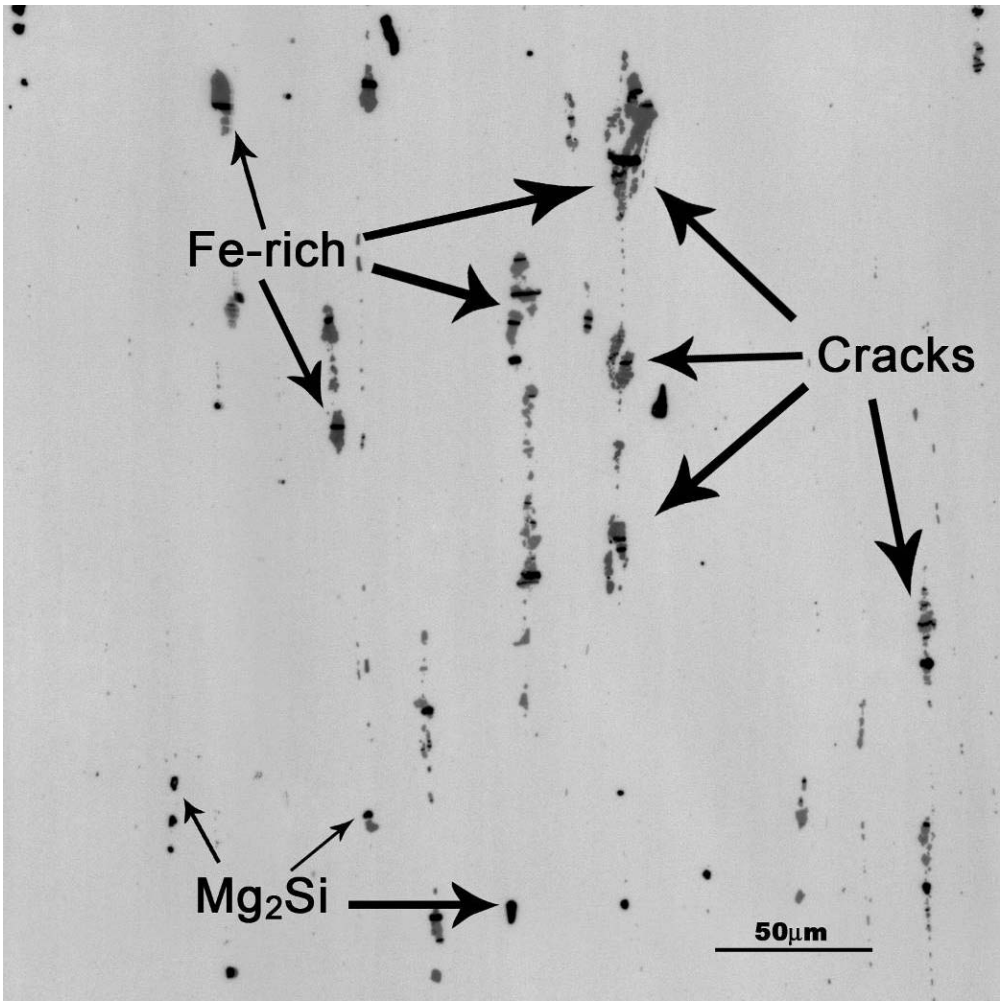

Figure 2 Microstructure Containing Cracked Fe-rich Constituent Particles.

Quantitative microstructural data on damage nucleation due to particles cracking are available on some 5xxx and 6xxx series wrought Al-alloys [12-14]. However, to the best of author's knowledge, detailed quantitative microstructural data on the cracking of coarse constituent particles have not been reported in the literature for important 7xxx series wrought Al-alloys such as 7075-T651 under monotonic loading conditions, and there have been no experimental quantitative microstructural data on any wrought Al-alloy on the particle cracking damage nucleation under cyclic loading conditions.

Quantitative characterization of particle cracking damage in these alloys has been problematic due to the following reasons.

1. Volume fraction of the constituent particles is small (~ 1%) and their spatial distribution is extremely inhomogeneous. Therefore, measurements on very large area of metallographic plane(s) are required to obtain reliable data. However, the size distribution of the constituent particles has a very wide range (~ 1 to 50 μm), particle morphologies are very irregular, and particle crack opening displacements are quite small (~ 0.5 μm), particularly under cyclic loading conditions. Therefore, the measurements have to be performed at a high magnification, and consequently, each field of view (FOV) is of very small area. Therefore, observations and measurements on very large number of microstructural fields (~ few thousand FOVs) are required. Further, depending on the applied stress and loading condition, etc. only a small percentage of the constituent particles may crack, which further increases the statistical microstructural sample size needed to obtain reliable quantitative data.
2. Digital image analysis and stereological procedures are not developed for automatic detection and measurements on cracked constituent particles. Therefore, manual detection of cracked particles and measurements on a large statistical microstructural sample are necessary, which are very tedious and time consuming.

Some of the above difficulties can now be overcome due to (i) advances in the image analysis procedures for automatic creation of “montages” of very large number of contiguous microstructural fields (~ 200 FOVs or more) at high magnification using an

automated microscope stage [15], (ii) recent developments in image segmentation procedures at Georgia Tech that permit automatic/semi-automatic detection of the cracked particles [16], which can decrease the efforts needed for detection of cracked particles very significantly, and (iii) development of C++ codes that utilize the binary microstructural images as input and measure even complex attributes such as two-point correlation functions, etc. in a automatic manner [17, 18]. Accordingly, the central objective of this research is to apply these recently developed digital image analysis and stereology based techniques for detailed quantitative characterization of the damage nucleation in hot-rolled 7075-T651 Al-alloy (a typical alloy of 7xxx series) due to cracking of the Fe-rich coarse constituent particles. The research mainly involves the following tasks.

- Quantitative characterization of cracking of Fe-rich constituent particles as a function of strain under quasi-static loading. This involves measurements of number density of cracked particles, volume fraction of the cracked particles, their size, shape, and orientation distribution, as well as nearest neighbor distribution and two-point correlation functions to quantify spatial dispersion of cracked particles in a series of interrupted uniaxial tensile test specimens at different strain levels.
- Quantitative characterization of cracking of Fe-rich constituent particles under cyclic loading to study the differences between the particle cracking damage due to monotonic and cyclic loading.

The next chapter of the thesis presents background on the microstructure and processing of 7xxx series alloys and digital image analysis and stereology techniques used in the

research. The experimental work and results and discussion are presented in the subsequent chapters.

CHAPTER II

LITERATURE REVIEW AND BACKGROUND

2.1 Introduction

The objective of this work is to quantitatively characterize the particle cracking damage in wrought Al 7075, and therefore it is of interest to study the history of the alloy, processing procedures, means of microstructural characterization, and damage modeling involving particle cracking data. The following section seeks to review literature on these topics. This information is used in the subsequent chapters for experiment design and implementation. Also, background on the microstructure and metallurgy of 7xxx series alloys and digital image analysis and quantitative microscopy are presented.

2.2 Background

7xxx series Al-Zn-Mg-Cu-base precipitation hardenable wrought Al-alloy products are widely used for aerospace structural applications where monotonic and cyclic mechanical properties are of prime concern [1]. The 7075 alloy possesses a tensile strength of approximately 83ksi which is higher than some steels. For this reason, the

alloy is used for highly stressed structural parts. It has good machinability, moderate corrosion resistance, and good anodizing response. The applications of 7075 alloy include: aircraft fittings, gears and shafts, fuse parts, meter shafts and gears, missile parts, regulating valve parts, worm gears, keys, commercial aircraft, and aerospace and defense equipment [19]. The following sections describe the chemistry, processing and microstructure of the alloy.

2.2.1 Chemical Composition

The composition of the Al-7075 alloy is Si (max .40%), Fe (max .50%), Cu (1.2-2.0%), Mn (max .30%), Mg (2.1-2.9%), Cr (.18-.28%), Zn (5.1-6.1%), Ti (max .20%), others each (max .05%), others total (max .15%), and Al (remainder). [19] Zinc and Magnesium are added to increase strength through the precipitation of very fine precipitates of the η' phase, a semicoherent metastable form of the equilibrium $MgZn_2$ phase. [20] The addition of copper strengthens the alloy primarily by solid-solution strengthening as well as precipitation strengthening. Chromium is added to improve the stress corrosion cracking resistance of sheets made from this alloy [21]. Manganese forms compounds that control grain structure and is also an effective strengthener on an atomic basis. Iron and silicon are impurities that form coarse intermetallic compounds such as the insoluble $Al_6(Fe,Mn)$, Al_3Fe, $\alpha Al(Fe,Mn,Si)$ and Al_7Cu_2Fe as well as soluble Al_2Cu, Al_2CuMg, and Mg_2Si. Coarse intermetallic particles such as these generally deteriorate fracture toughness, fatigue resistance, and ductility [22].

Table 1 Chemical Composition of Wrought 7075 Al-Alloy [19]

Percent Weight	Elements										
	Si	Fe	Cu	Mn	Mg	Cr	Zn	Ti	Others Each	Others Total	Aluminum
Minimum	-	-	1.2	-	2.1	.18	5.1	-	-	-	
Maximum	.40	.50	2.0	.30	2.9	.28	6.1	.20	.05	.15	Remainder

2.2.2 Processing

Roughly 85% of aluminum is used for wrought products which are produced from cast ingots. The mechanical properties of the wrought Al-alloys can be dramatically changed by various working operations and thermal treatments. First, virgin aluminum, scrap and alloying additions are melted in a furnace and mixed with fluxing, degassing and filtering to remove dross, oxides, gases and other non-metallic impurities. To remove porosity, it is necessary to reduce hydrogen (rejected from liquid metal upon solidification) to less than .15 cm^3 per 100g. Direct-Chill (DC) processing is used to obtain a desirable uniform ingot structure. DC takes place in two steps, cooling from chilled mold walls followed by spray cooling. The resultant ingot has rectangular cross section and is suitable for rolling (or forging or extrusion). It is necessary to machine the surfaces of the ingot to remove surface tears or rippling prior to rolling. Also, homogenization at a temperature in the range of 450-600^oC is used to reduce microsegregation effects, to remove non-equilibrium, low melting point eutectics (which may crack in working) and to control precipitation of excess concentrations of elements. Most ingots are heated for 10 to 24 hours prior to hot working. The ingots are then hot-worked to achieve uniform grain size, annealed, and rolled usually with a reduction of area for each pass. Hot rolled alloy is annealed and then it may be cold rolled to the final dimensions. Precipitation hardening thermal treatment is finally carried out by solution

treatment, quenching, and ageing to achieve the desired mechanical properties. [22] Strengthening occurs through precipitation involving the following precipitation sequence:

Supersaturated Solid Solution → GP Zones → η'($MgZn_2$) → η($MgZn_2$)

The GP zones are spherical and coherent with the matrix, the intermediate metastable phase, η', has monoclinic unit cell, and the incoherent equilibrium phase, η, is hexagonal. Duplex aging may be used to obtain high strength by first aging for 5 days at 20°C (i.e. natural aging) and then 48 hours at 120°C. The first step creates a narrow size distribution of small stable GP zones, and the second step dissolves some GP zones while growing others. Aging at higher temperatures results in coarser precipitates, while single stage aging produces a fine dispersion of η' precipitates with wide precipitate-free zones. Overaging and coarsening of precipitates lowers the ultimate tensile strength [21].

2.2.3 Microstructure

Microstructural features that control the mechanical behavior include coarse intermetallic compounds (constituent particles) of size greater than .5μm, submicron dispersoids of size less than .5μm, fine precipitates of sizes up to .1μm, dislocation substructures, matrix grains of different sizes and shapes, and crystallographic textures due to plastic deformation and annealing. [22] The microstructure of a typical hot-rolled, precipitation hardened 7075 alloy consists of Al rich grains, fine Mg_2Si precipitates and coarse Fe-rich and Mg_2Si particles (typically in the size range 1 – 50 μm) [2,3]. The Fe-rich Al_7Cu_2Fe and $(Al,Cu)_6(Fe,Cu)$ are the most abundant intermetallics while Mg_2Si is present in less abundance [23-25]. Other particles and precipitates formed

are $MgZn_2$, $Mg_3Zn_3Al_2$, Mg_5Al_3 [2]. Figure 1 shows microstructure of a hot-rolled 7075 Al-alloy depicting the coarse constituent particles. In this microstructure, the dark equiaxed particles are Mg_2Si particles, where as the gray particles are the Fe-rich intermetallic constituent particles. Observe that the Fe-rich constituent particles have complex shapes/morphologies; they are spatially non-uniform (clustered); and have partially anisotropic morphological orientations.

2.3 Damage Evolution

It has been well established that plastic deformation and fracture of 7xxx series alloys (as well as of numerous other wrought Al-alloys) is associated with the gradual microstructural damage accumulation that involves cracking of the coarse constituent particles, growth of voids around the cracked particles, and void coalescence [4,5,6,7,8]. For this reason, it is of interest to first study the mechanisms controlling particle cracking. Many damage models have been proposed to predict particle cracking [4,26-43]. These models can be organized by their failure criterion, namely: energy, stress, or strain. Also, these models are derived differently using dislocation theory or continuum mechanics. Because of the large variations between proposed models, it is important to further study the particle cracking behavior. However, general guidelines from such studies [4,5,6,32,36,37,45] include:

- as particle size increases, the stress required for cracking decreases
- for the most part, cracking occurs after plastic deformation
- cracking increases with both stress and strain

- most cleavage planes are perpendicular to the loading (tensile) direction
- elongated particles are more likely to crack than equiaxed particles

Gurland and Plateau [4] studied the mechanics of crack nucleation at inclusions to develop a relationship between inclusion characteristics and fracture ductility using aluminum casting alloy, Armco iron, and pearlitic steel. They defined the necessary condition for cracking to be that the strain energy stored at the inclusion, *U*, is greater than or equal to the surface energy of the new crack faces, *S*. They derived the following equation:

$$\sigma = \frac{1}{q}\left(\frac{E\gamma}{a}\right)^{\frac{1}{2}} \qquad (2.1)$$

where σ is the applied uniaxial stress, q is the average stress concentration at the inclusion, γ is the specific surface energy of the crack, E is a weighted average of the elastic moduli of inclusion and matrix, and a is the dimension of the inclusion. Therefore, the stress required to crack an inclusion is inversely related to the size of the particle.

Lindley et al [36]. proposed a fiber-loading mechanism where the maximum stress, σ, in an elongated particle is obtained from the following equation:

$$\sigma = \alpha\tau \qquad (2.2)$$

where α is the aspect ratio and τ is the matrix shear stress. Therefore, the maximum stress is directly proportional to the aspect ratio of the particle, and more elongated particles will have a larger maximum stress and be more likely to crack.

Yeh and Liu [32] studied the cracking of Si particles in an age-hardenable A357 alloy with the objective of better understanding the cracking phenomenon and the mechanism of inclusions. They concluded that based on the dislocation pileup mechanism, the relationship existed that:

$$\frac{F}{T} = \frac{ADm^2L^2M^5\sigma^5(\varepsilon - \varepsilon_0)}{5n+1} \qquad (2.3)$$

where *F/T* is the fraction of cracked particles, *A* is a constant, *D* is the particle size, *m* is the pileup number in a slip band, *L* is the pileup length, *M* is the Schmid factor, σ is the applied true stress, ε is the applied true strain, and ε_0 is the true strain at which yielding occurs. Therefore, the fraction is directly proportional to the particle size, true stress and true strain. They also concluded that the fraction of cracked particles was related to the cleavage plane by the following relationship:

$$\frac{F}{T} \propto [\sin 2(\Phi - 45°)]^5 \qquad (2.4)$$

where Φ is the angle between the applied tensile axis and the cleavage plane. The results of this work were in good agreement with that of Gurland [44].

2.4 Digital Image Analysis

Microstructures are three-dimensional (3D) and therefore their 3D geometric properties are of interest. Furthermore, many material microstructures, such as aluminum, are opaque and must be characterized by estimating three-dimensional properties from two-dimensional probes such as the metallographic plane. To measure properties from these two-dimensional metallographic sections, one uses an image analysis system consisting of a computer, which processes images and makes measurements, and an interface, which transfers images from the camera to the computer. The interface is usually a CCD camera. Also, the system may contain peripherals such as an automatic stage or auto-focusing mechanism for efficiency.

A digital image is a pattern of pixels which may be either RGB (red, green, and blue channels) or grayscale (single channel). Each channel is marked with values ranging from 0 to 255, 0 denoting black and 255 denoting white. An image is stored as a pixel map, recording the location and corresponding gray value(s) of each pixel. Digital image analysis involves taking a grayscale or color image and converting it to a binary image (2 colors, 0 for black and 255 for white). This process is called thresholding (or segmentation). The color or grayscale image is segmented by a user defined value. Every pixel having a gray value higher than the selected threshold value is set to white, and every pixel having a gray value less than the selected threshold value is set to black. In this manner, the binary image is created, which can be used for subsequent measurements. Using a calibration slide, one can determine the magnification scale factors for both x and y directions (may be different depending on type CCD). Finally,

one can export the measured data to a spreadsheet program such as Microsoft Excel to determine mean values and standard deviations of the geometric properties of interest [15].

2.4.1 Montage Creation

For statistical reliability, measurements must be performed on a large statistical sample. This can be achieved by performing measurements on a large number of independent microstructural fields. However, such sampling can introduce bias due to edge effects. The bias can be minimized by using large area montages at high resolution. A montage can be created by stitching contiguous fields of view. The stitching is done using overlapping regions to ensure individual fields of view are aligned to create a seamless montage. The resultant image has a high resolution (.20325 μm/pixel) and a large area (1.5 mm^2) and is free of edge effects. The large area montage contains information about both long and short range spatial patterns. As a result of using this procedure, resolution is sufficient to capture complex particle morphologies and fine cracks within particles. An automatic stage is used and in the present work an initial field of view is arbitrarily chosen. The image analyzer saves the first image into memory, moves the stage to the next position, uses an auto-focus procedure, saves the next image into memory and so forth. Once all the images are saved into memory, a stitching software automatically utilizes overlapping regions to align adjacent fields of views. For a microstructure containing a very low volume fraction, difficulties in stitching images results from empty overlapping regions. One must have an accurate stage (a mechanical system's accuracy deteriorates with use) to eliminate stitching errors. Figure 3 shows a

typical digitally compressed montage of 225 contiguous fields of view grabbed at an 80X objective magnification (1 pixel / .20325 μm).

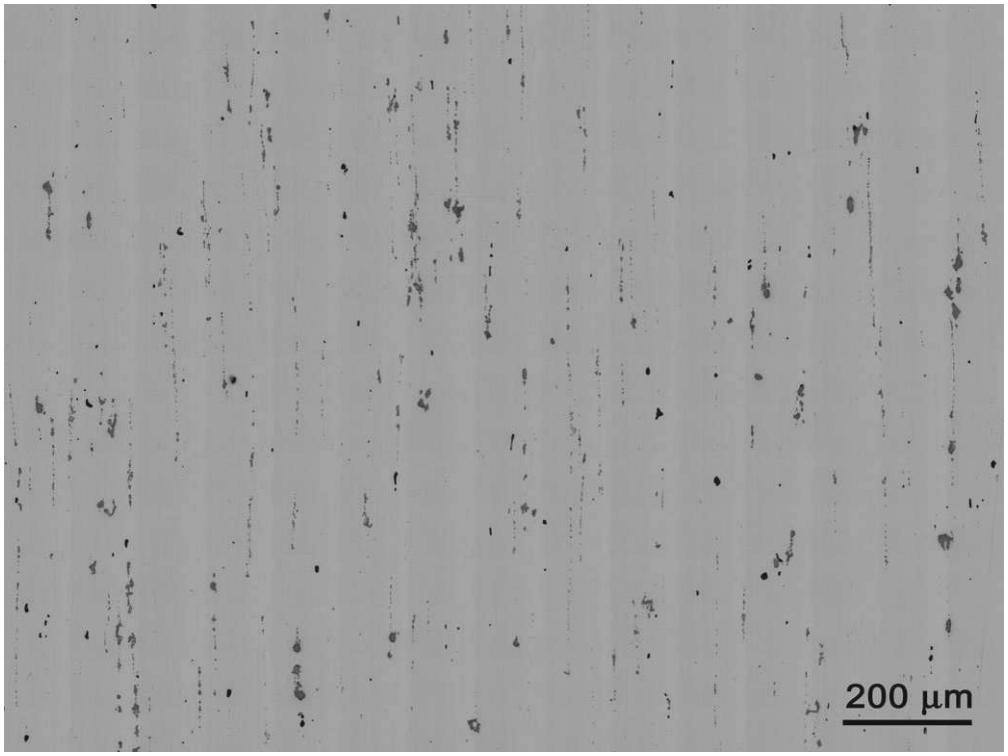

Figure 3 Digitally Compressed Montage of 225 Contiguous Fields of View.

2.5 Quantitative Microscopy

The objective of quantitative metallography or stereology is to describe the geometric characteristics of the microstructural features of interest using quantitative mathematical descriptors to answer such questions as how much, how many, and how big or small.

Because microstructures are three-dimensional and as a result their attributes and features are three-dimensional and most materials are opaque, one must estimate three-

dimensional properties from two-dimensional information such as the microstructural image observed in a metallographic plane. Such a microstructural image is comprised of the intersections of three-dimensional features with the metallographic plane. Because this two-dimensional view does not contain all the information relevant for three-dimensional microstructural space, one can not estimate all three-dimensional properties from two-dimensional information. However, many important three-dimensional microstructural descriptors can be accurately estimated from measurements made on two-dimensional metallographic sections [46]. The basic stereological procedures used for estimating three-dimensional geometric parameters are described in the sections that follow.

2.5.1 Number per Unit Area

One important parameter in process-microstructure-properties studies is the number of microstructural features of interest per unit area, N_A. It can be estimated by counting the number of those features per a given area of a metallographic plane. In this manner a count/area can be established. An efficient and unbiased counting technique has been developed to eliminate bias due to edge effects. This method of "forbidden edges" involves counting features completely inside a microstructural frame, counting any lying on a 2 arbitrary edges, and *not* counting any on the other two edges [47]. Another way to minimize the edge effect is to considerably increase the area of the microstructural frame such as with the montage technique. By considering an area which is 25-100 times the size of a single microstructural field of view, the bias of edge effect can be minimized.

In general, three-dimensional number densities cannot be estimated from independent random two-dimensional sections. However, previously, it has been shown in a similar experiment using a similar material [48] that for a tensile loading condition parallel to the rolling direction that there is good agreement between the two-dimensional number fraction and the three-dimensional number density of cracked particles. For this reason, this work measures the two-dimensional number fractions for a great time savings.

2.5.3 Volume Fraction

Numerous properties of materials depend on the volume fraction of different phases in the microstructure. The volume fractions depend on both chemistry and processing history of the material. The volume fraction is the numerical extent of the amount of a phase (or constituent) in a given unit of volume of three-dimensional microstructure and is denoted as V_V. Because of the normalization by volume, the volume fraction is a dimensionless parameter. Image analyzers use areal analysis as they can quickly calculate the number of pixels of a given phase per total number of pixels contained in an image. Manually, one can use point counting or lineal methods to estimate the volume fraction. The point counting procedure involves superimposing a test grid on the microstructural image and counting the number of points (at vertices) contained in the feature of interest per total number of points on the grid, P_P. The average value of P_P is equal to the volume fraction. The lineal analysis method involves superimposing a set randomly placed straight test lines on the microstructural image and measuring the lengths of those lines contained in the phase of interest per total length of

test lines, L_L. The average value of L_L is equal to the volume fraction. It should be noted that the volume fraction of any one phase in a microstructure must fall in the range $0 \leq V_V \leq 1$. In addition, the summation of the volume fractions of all phases must be equal to one [46].

2.5.4 Two-Point Correlation Function

In a two phase microstructure, the two-point correlation function, $P_{11}(r, \theta, \phi)$, is defined as the probability that a randomly placed line of angular orientation (θ, ϕ) and length r will have both endpoints in the phase denoted as 1. In this manner, for a two phase microstructure one could develop four two-point correlation functions, $P_{11}(r, \theta, \phi)$, $P_{22}(r, \theta, \phi)$, $P_{12}(r, \theta, \phi)$, $P_{21}(r, \theta, \phi)$. However, only one of which is independent. Defining V_1 as the volume fraction of phase 1 and V_2 as the volume fraction of phase 2, the following relationships exist:

1. $P_{11}(r, \theta, \phi) + P_{12}(r, \theta, \phi) + P_{21}(r, \theta, \phi) + P_{22}(r, \theta, \phi) = 1$ (2.5)

2. $P_{12}(r, \theta, \phi) = P_{21}(r, \theta, \phi)$ (2.6)

3. $P_{11}(r, \theta, \phi) + P_{12}(r, \theta, \phi) = V_1$ (2.7)

4. $P_{21}(r, \theta, \phi) + P_{22}(r, \theta, \phi) = V_2$ (2.8)

As r approaches infinity, (2.9)
$P_{11}(r, \theta, \phi)$ approaches V_1^2 and $P_{22}(r,\theta,\phi)$ approaches V_2^2

As r approaches 0, (2.10)
$P_{11}(r, \theta, \phi)$ approaches V_1 and $P_{22}(r, \theta, \phi)$ approaches V_2

If the microstructure contains a symmetry axis and if one chooses this axis as the z-axis, the function does not depend on ϕ and it is simplified to $P_{11}(r, \theta)$. Note that $P_{11}(r,$

θ) measured in any one vertical plane completely specifies the direction dependence of the two-point correlation function.

For the two-point correlation function to capture both short range and long range information, for most microstructures, one must estimate it over the distance range 1 to 500 μm at a resolution of .5 μm. Therefore, the two-point correlation function is impossible to calculate from one single field of view (which may only have a large area or a high resolution but not both). The montage technique, developed earlier, can be used to create large area images of seamlessly stitched single fields of view to meet these requirements.

Measurement of two-point function is computationally intensive, and for this reason a computer code has recently been developed [49]. The program input is a binary image and a user defined maximum length, l_m. The program takes a virtual frame inset by the distance l_m from the original image, denoted as the measurement frame, to make measurements on. This eliminates edge effects created by particles within the distance l_m from the edge of the image where the two point function cannot be calculated. The program then measures the gray value of the starting pixel or base point (0 or 255) and the gray value for each pixel inside the circle of radius l_m. This process is repeated for each and every pixel inside the measurement frame. Once all measurements are made, the probability is computed by dividing the number of segments whose endpoints are both black by the total number of line segments. The process is then repeated for each and every line segment length and orientation [46].

2.5.5 Nearest Neighbor Distribution Functions

The nearest neighbor distribution functions are important quantitative descriptors of short, intermediate and long range order of special arrangements. The first nearest neighbor distribution function is defined as the probability density function $\psi_1(r)$, such that $\psi_1(r)dr$ is the probability that there are no other particles in the sphere of radius r around the particle center, and that there is *at least* one particle center in the shell of radii r to (r+dr) around the same particle center. The second nearest neighbor distribution function is defined as the probability density function $\psi_2(r)$, such that $\psi_2(r)dr$ is the probability that there is *exactly* one particle center in the sphere of radius r around the particle center, and that there is *at least* one particle center in the shell of radii r to (r+dr) around the same particle center. The n^{th} nearest neighbor distribution function is defined as the probability density function $\psi_n(r)$, such that $\psi_n(r)dr$ is the probability that there is *exactly* n particle centers in the sphere of radius r around the particle center, and that there is *at least* one particle center in the shell of radii r to (r+dr) around the same particle center. Therefore, as n increases, the nearest neighbor function contains information from the short range to long range spatial patterns. In general, three-dimensional information about nearest neighbor distributions cannot be gathered from random independent two-dimensional metallographic sections [46].

CHAPTER III

EXPERIMENTAL WORK

3.1 Introduction

The objective of this work is to quantitatively characterize the microstructural damage evolution due to cracking of iron rich intermetallics (constituent particles) under monotonic and cyclic loading in a wrought aluminum alloy. This chapter describes the experimental set up and procedures. The following sections seek to provide basic descriptions of experiment design, metallographic techniques, image analysis and stereological procedures used. The microstructural data obtained from these experiments are analyzed in the next chapter.

3.2 Provided Material

Experiments were performed on both round and rectangular tensile bar specimens cut from hot-rolled Al-7075-T651 plates. The chemical composition is given in Table 1. The metallographic specimens were cut such that the rolling direction was oriented parallel to the direction of loading. In the rolled alloy, microstructure contains elongated

Fe-rich particles with both Fe-rich and Mg_2Si particles aligned in stringers parallel to the rolling direction.

3.3 Mechanical Testing

Mechanical testing was performed at Northrupp Grumman Corporation. Rectangular tensile bars were uniaxially strained and interrupted in seven incremental strain values (up to 14.96% absolute strain at failure). The loading was parallel to the rolling direction. Round tensile bars were uniaxially fatigued at both high (.0075) and low (.0025) strain amplitudes and interrupted in incremental number of cycles (up to failures of 2311 and 425,100 cycles, respectively). The loading was also parallel to the rolling direction. These tests were performed to study the particle cracking behavior as a function of applied strain and number of cycles. The following sections detail the test specifics.

3.3.1 Uniaxial Tensile Tests

Tensile tests on 7075-T651 aluminum were conducted using a dog-bone type tensile coupon designed based on the ASTM standard (E8). The specimen geometry and dimensions are given in Figure 4. The dog-bone type specimens were machined from the outer layer of the 5.08 cm (2 in.) thick 7075-T651 aluminum plate, in the longitudinal direction, .3175 cm (.125 in.) from the face of the rolled plate. The tensile tests were conducted using Tenuis Olson type tensile machine. The tests were conducted at a constant cross-head control of 12.7 cm (5 inches) per minute. A MTS knife blade axial

extensometer with a 5.08 cm (2 inch) gage length was used for the strain measurements and was set at a full scale of 25% strain and calibrated to better than 1% through the full-scale range. The load cell was calibrated to within 1% error reading through the full-scale range. The stress strain data were collected on a System 5000 Data Acquisition system. Tensile tests were interrupted at incremental percentages of total failure strain.

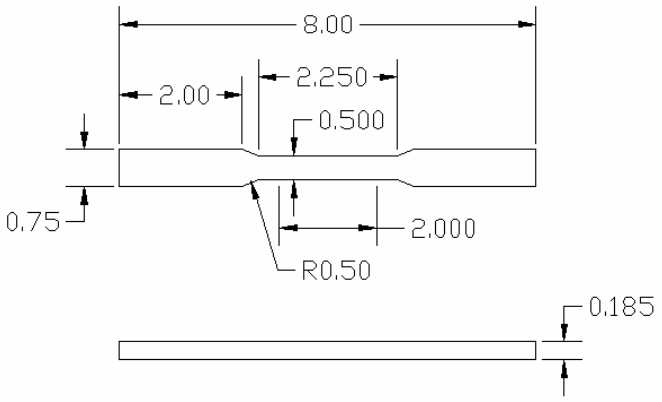

Figure 4 Geometry of Tensile Coupon Based on ASTM Standard E8.

3.3.2 Fatigue Tests

Strain-controlled fatigue tests were conducted on 7075-T651 aluminum using 2.54 cm (1 in.) diameter cylindrical specimens machined from the outer layer of a 5.08 cm (2 in.) thick plate, in the longitudinal direction. Cylindrical fatigue specimens, as shown in Figure 5, were designed based ASTM standards [E 647-99] with a slight modification in the gage section. To induce fatigue failure in the gage section, a small uniform change in diameter, similar to an hourglass design but having a much larger radius, was introduced in the gage section. The specimens were cut from the outer layer of the plate so that the center line of the each specimen was 1.43 cm (0.5625 inch) from

the free surface of the plate and machined so that the rolling direction was parallel to the loading axis. Residual stress measurements were performed on specimens before and after polishing using X-ray diffraction. The fatigue testing set-up had cylindrical collet grips to ensure proper alignment of the specimens. The frames were aligned to within .254 mm (0.001 inch) of deflection. Load cells were calibrated to within 1% error reading through the full-scale range. A MTS fatigue rated knife blade axial extensometer was used for the strain measurements. The extensometers were set at a full scale of 2% strain and calibrated to better than 1% for the full scale range. The MTS controller application, called MPT, was used for programming, control and data collection. The tests were performed at strain amplitudes 0.0025 and 0.0075.

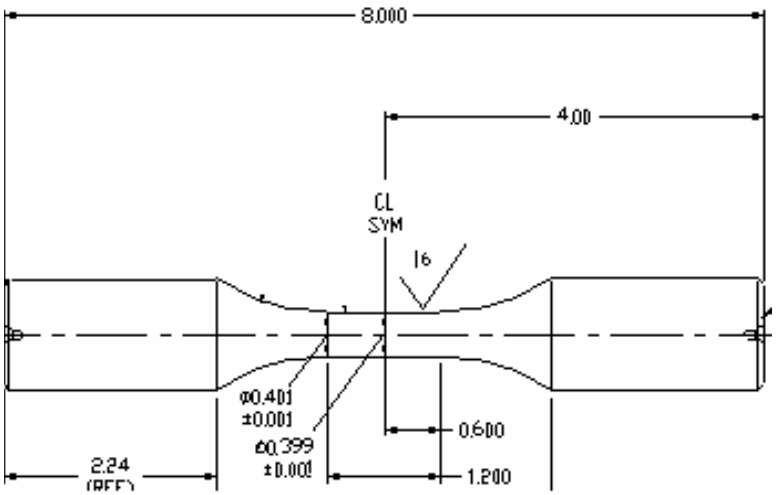

Figure 5 Geometry of Cylindrical Fatigue Specimen Based on ASTM Standard E647-99

3.4 Metallography

Because the Al 7075 microstructure is opaque, methods for obtaining information about the microstructure are limited to two dimensional probes, such as the metallographic planes. This section contains information about how metallographic samples were prepared through cutting, mounting, grinding, and polishing procedures.

The microstructure of a rolled aluminum plate is anisotropic, and consequently, the measurements must be made on carefully selected planes to capture the features of interest. For example, a plane perpendicular to the tensile direction will for all practical purposes not depict a cracked particle due to the infinitesimal chance of intersecting a cracked plane that is parallel to it. For this reason, each tensile test specimen was first cut along the L-S plane containing the rolling and thickness directions. It is in this plane that particle shapes and cracks are most clearly visible. Figure 6 depicts the orientation of planes for the rolled microstructure. From each strain specimen, a section inside the gage length of the L-S plane was cut using a precision saw to observe the cracked particles. For each fatigue specimen, the L-S plane was first cut through the length of the round bar using Electrical Discharge Machining. Finally, a precision saw was used to cut sections from the gage length. Also, to study the unstrained material, for each set, a grip section was cut from the lowest strain sample.

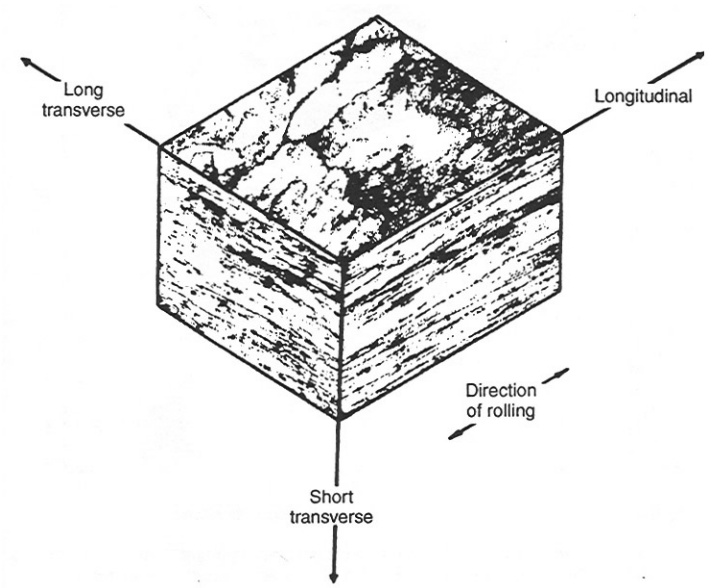

Figure 6 Orientation of Planes for a Rolled Microstructure [59].

After sectioning is complete, mounting is required for subsequent handling and polishing of the metallographic specimens. The polishing procedure requires that the final surface accurately represent the structure of the material before sectioning. To this end, grinding is first used to remove scratches and machine marks generated by the cutting saw during cutting. This is followed by polishing to remove fine scratches and to obtain a highly reflective shiny surface. Optical microscopy uses reflected light to detect microstructural features, and therefore, a highly reflective surface is required. The difference between grinding and polishing is that grinding employs the use of fixed abrasive particles, whereas polishing employs the use of smaller abrasive particles in suspension. The complete procedure is detailed as follows. First the cut sections were mounted in standard 1¼" diameter epoxy mounts, chosen so that multiple samples could be prepared quickly and simultaneously. Initial grinding followed a progression of 240, 320, 400, 600, 800 grit silicon carbide papers at low pressure (to avoid particles from being embedded in the matrix) while continually flushing with water. Polishing followed

with lapping cloths beginning with 6 μm diamond suspension, followed by 3 and 1 μm diamond suspensions, and finishing with a colloidal silica solution. To obtain a clean stain free surface, each polishing step was finished by flushing with water for 15 seconds followed by flushing with ethanol for 15 seconds and blow drying. Once the required metallographic finish was obtained, observations were made on unetched samples using an optical microscope. Figure 7 shows a single field of view taken from the prepared sample. Observe two gray value distinguishable types of particles, those of light gray color (Fe-rich) and those of nearly black color (Mg_2Si).

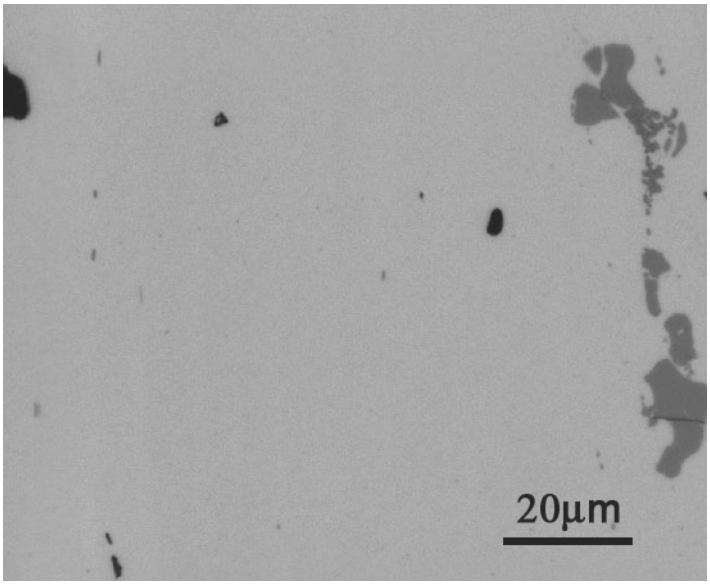

Figure 7 Single Field of View with Pixel Size of .19 μm.

3.5 Digital Image Analysis

Digital Image Analysis is the process by which one captures microstructural images and then extracts quantitative information from them. First, montages were created using the procedure described earlier. A Zeiss optical microscope with automatic stage and AxioVision image analysis software package were used for montage creation.

Figure 3 shows a digital large area montage of compressed 225 seamless fields of view grabbed at an 80X objective (50X + 1.6 optivar lens) that has a resolution of .19 μm per pixel size. The method for obtaining such large area montages was described in Chapter II. Quantitative measurements were performed on the montages using the Zeiss KS400 image analysis software. The following sections detail the different procedures for separating cracked particles in the microstructure and measurement procedures.

3.5.1 Automatic Separation of Cracked Particles in Tensile Test Specimen

Figure 8 shows a typical field of view of the microstructure of the tensile failure specimen containing cracked Fe-rich particles. Observe that cracks in strained samples appear as thick very dark lines that are mostly perpendicular to the tensile direction. Because these cracks have high contrast and are relatively thick, it is possible to automatically separate particles containing them. The computer code and image analysis procedure for automatic detection of cracked particles has been developed by Yuxiong Mao of our research group. Figure 9 illustrates the following process. The first step in the procedure involves segmenting the original image into the color regions of interest (A→B+C). Then, boundaries are traced from the binary images (B→D/C→E). Next, using relative amounts and orientations of the lighter regions (E) of certain gray value ranges within each boundary, particles are automatically separated as either Mg_2Si or Fe-rich particles. Subsequently, using amounts and orientations of the dark regions (D) within the Fe-rich phase, cracked particles are separated from the undamaged Fe-rich particles (F). Thus, three sets of resultant images are obtained: one set containing only cracked particles (F), the second containing all Fe-rich particles, and the third containing

only Mg_2Si particles, distinguished by gray values on a white background. Each resultant montage is a large image (typically 50MB). It takes under a minute to automatically create each of these segmented montages.

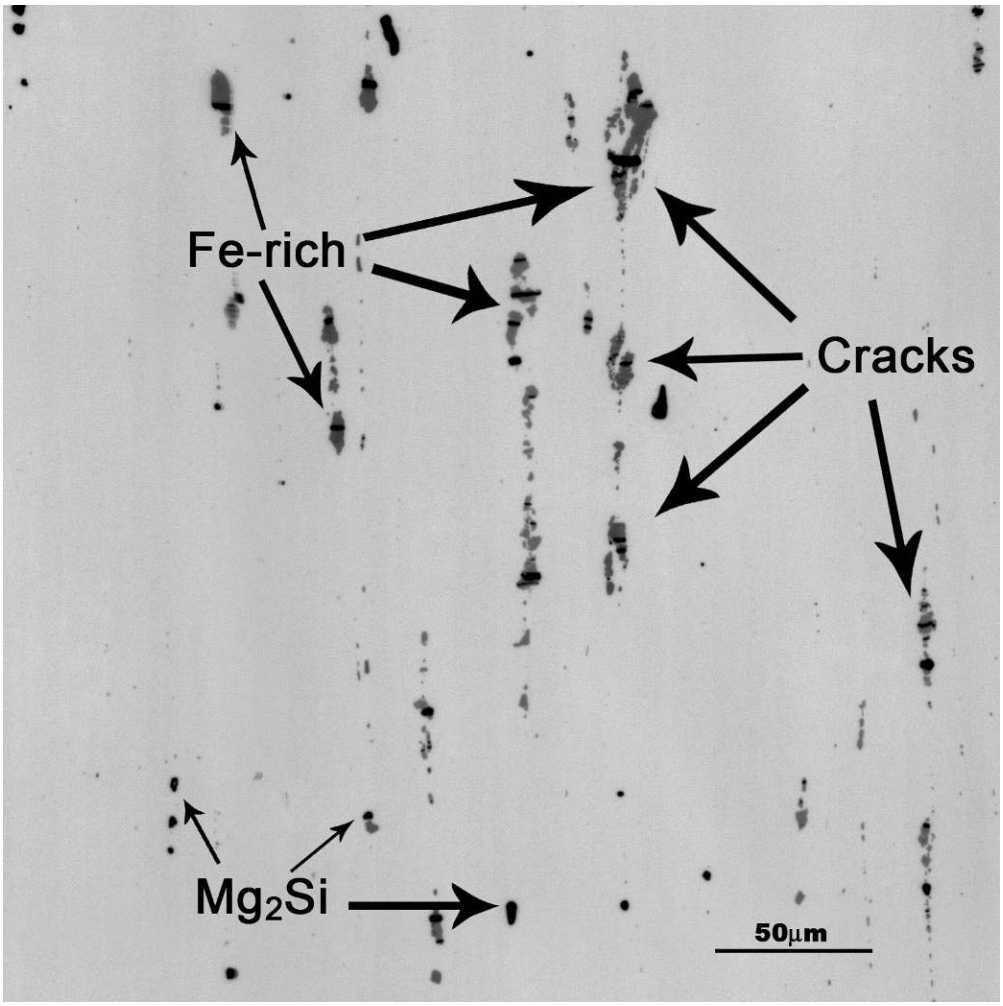

Figure 8 Microstructure of Tensile Failure Specimen.

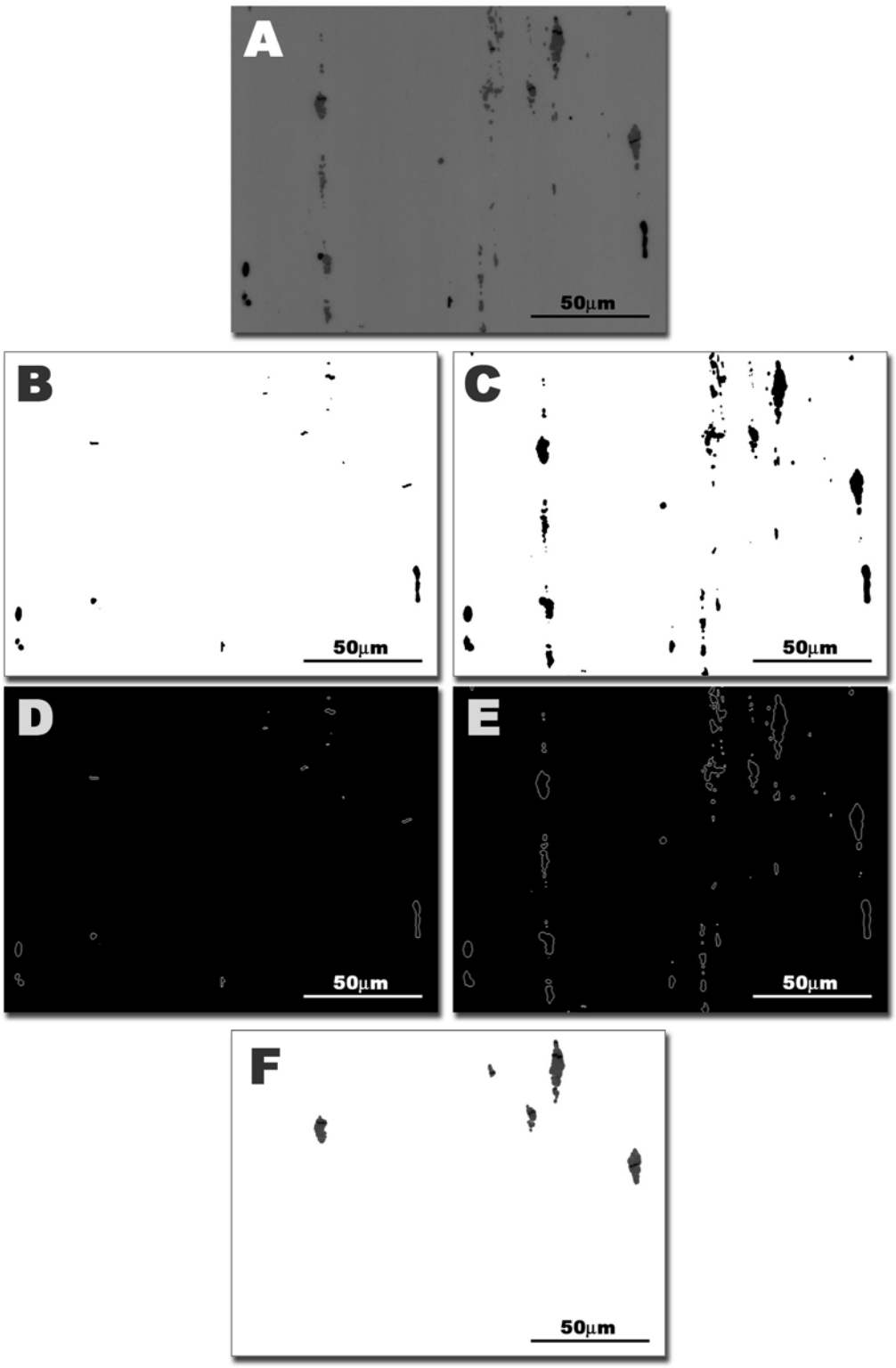

Figure 9 Automatic Separation of Cracked Particles Procedure.

3.5.2 Segmentation of Cracked Particles in Fatigue Test Specimens

Figure 10 shows a typical microstructural field of view in a fatigue failure specimen. Observe that cracks in strained samples appear as thin dark lines perpendicular to the tensile direction as opposed to thick dark lines in tensile test specimens. Because fatigue cracks are lighter and much thinner than cracks developed under higher strains (possibly due to crack closure), the procedure for automatically detecting cracked particles is not as accurate and must be combined with interactive manual methods. First, images are produced from in-house C codes using the method described for tensile test specimens to serve as a starting point. For manual confirmation of cracked particles, a procedure was developed utilizing Photoshop CS and its action capabilities. The results from automatic detection of cracked particle images are overlaid on the original grayscale image with a blend mode set to *difference*. This difference mode sets resultant pixel values by subtracting the gray values of the two separate layers. Therefore, any pixel value shared by both images appears as black and regions of difference appear as varying light shades depending on their difference. The main steps are as follows. By setting Photoshop CS actions to overlay a grid to serve as a place holding guide, automatically select a user defined particle using the “magic wand” tool and duplicate that particle on to a separate layer, move and merge that new layer with the edited cracked image, the process of manually adding and removing cracked particles from the image is quite efficient. Each resultant layered image is on the order of 100MB and is automatically created using Photoshop batch and action features. Once flattened to a single layer these images are on the order of 50MB and each image takes between 5-10

minutes to manually check and create (depending on number of cracked particles). Figure 11 illustrates this process.

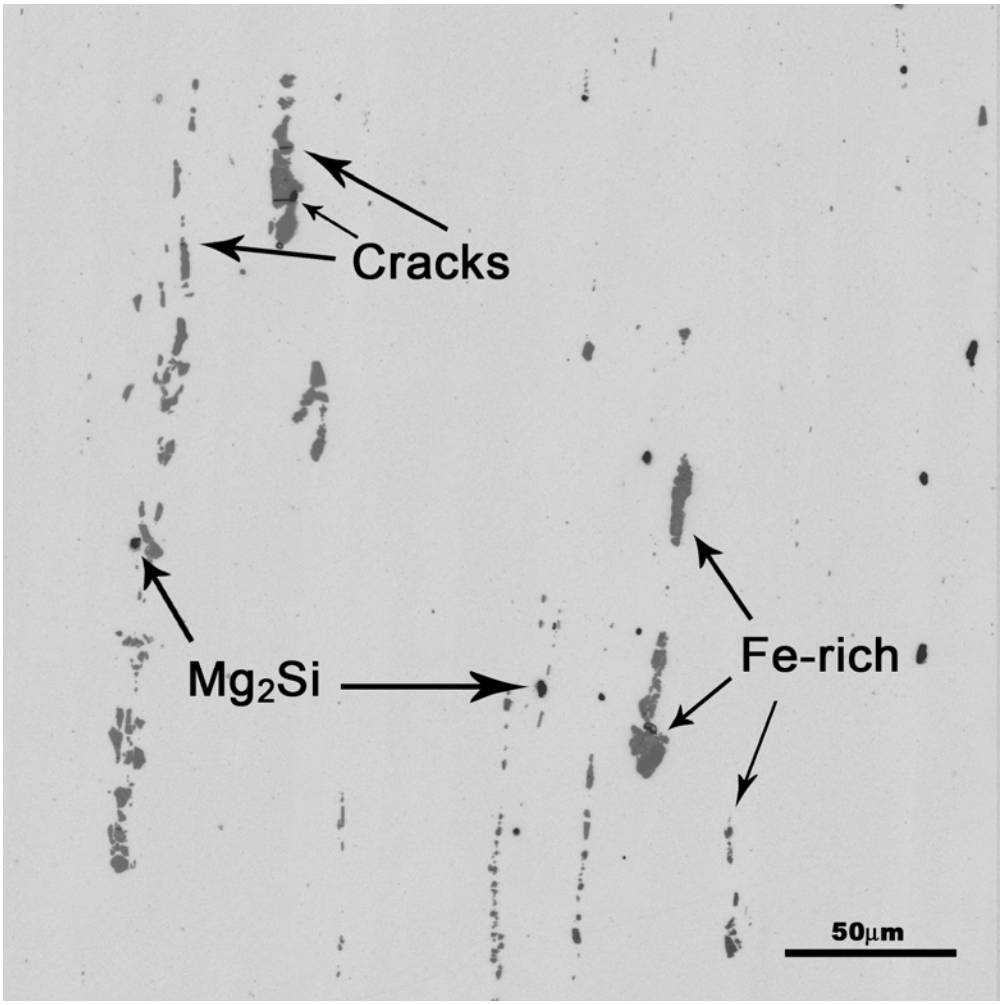

Figure 10 Microstructure of Fatigue Failure Specimen.

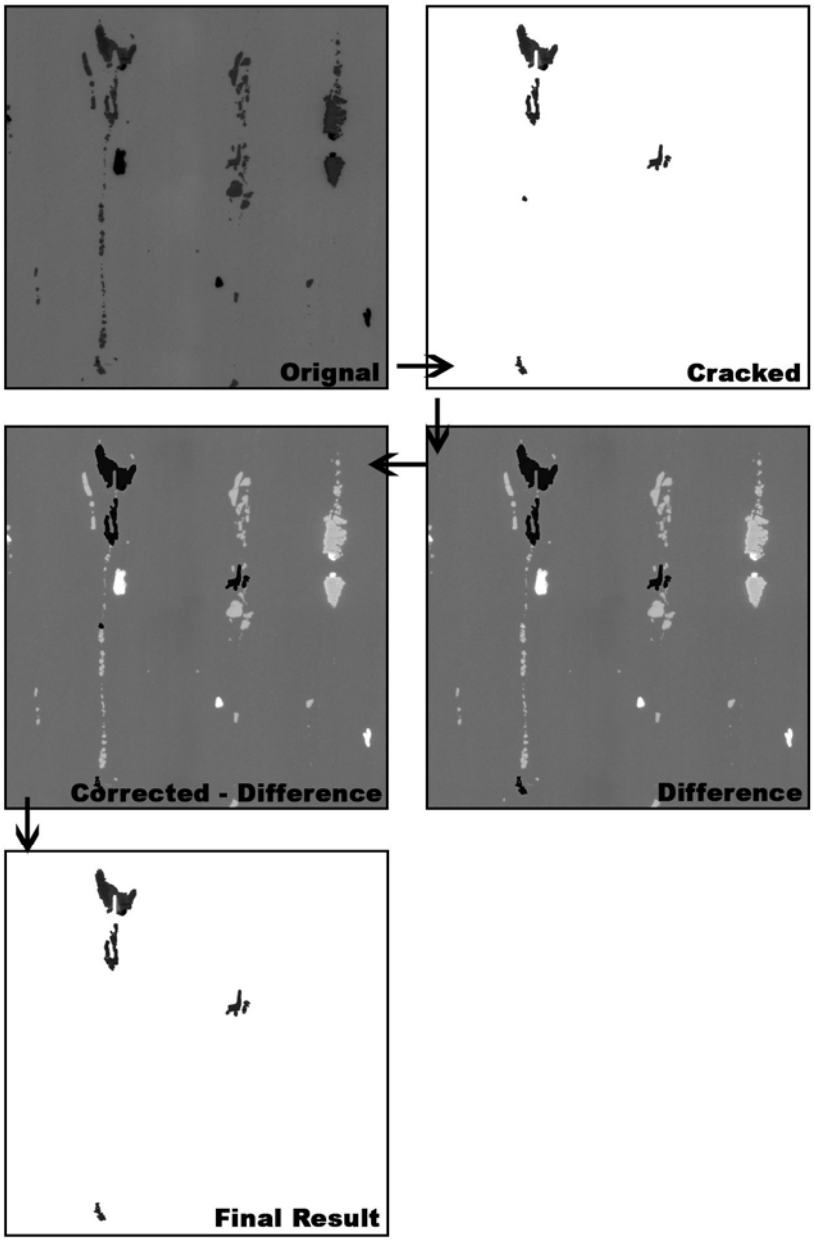

Figure 11 Photoshop Procedure for Fatigue Specimens.

3.5.3 Measurements

Once the cracked particles are segmented, one needs to extract quantitative information from the images. KS400 was used to generate microstructural data from the segmented images. The parameters such as maximum and minimum feret diameter sizes,

areas, perimeters, particle centroids and angular orientations have been measured for each set of particles. Each image is first segmented (thresholded) or converted into a binary image. Any pixel with a gray value less than the threshold value is set to black and any pixel with a gray value more than the threshold value is set to white. From the segmented image, measurements are then made and exported to a spreadsheet software such as Excel. The process of measuring multiple images was also automated using macros and AutoIt script (autoitscript.com) so that, once automated, measurements on approximately 400 images could be made in a days time.

3.6 Quantitative Microstructure Characterization

To understand and model the microstructural damage evolution processes, quantitative microstructural data associated with particle cracking are required. For this reason, microstructural parameters such as area fraction, size and orientation and spatial arrangement of both cracked and uncracked particles were measured using above image analysis techniques. Large area montages were taken on the L-S plane, so that cracks and particle morphologies could be most easily resolved, at a high resolution (.20μm/pixel) and statistically robust information could be obtained for both short and long range patterns.

In performing the measurements, one important issue is scrapping. Scrapping is the process by which one eliminates some (irrelevant information) “noise” from the “information” contained in the microstructural field. Scrapping is the removing of irrelevant information, in this case, the decision of what constitutes a particle. This step

is important because by removing particles based on their sizes (a certain number of pixels) one can drastically change the estimated properties such as number per unit area. This is particularly so, if the size distribution contains large number of very small particles. The procedure presented here uses a scrapping level of 25 pixels or approximately $1\mu m^2$ area. This level was determined by the resolution of the image and what size particles we expect to be able to detect. Particles are on the size range of 25 pixel area have varying gray values due to the resolution and one cannot be certain as to what phase they contain, not to mention, whether they are actually particles.

A second important issue is the amount of material needed to accurately characterize the microstructure. To ensure that a robust data set is achieved, the first data collected on tensile specimens were analyzed to determine the acceptable number of cracked particles required to achieve repeatable results. For the lowest strained specimen (3.71%) one would expect the smallest number of cracked particles. Measurements made on approximately $30mm^2$ area of metallographic planes were divided into three separate independent groups, each containing 600+ particles (number fractions of approximately 7.5%). The error between number fractions was 4-9%. It was therefore assumed that 600 cracked particles would be adequate as a minimum and three times that acceptable. Furthermore, because the amount of damage was higher for tensile specimen, measurements for the fatigued specimens were made over approximately $90mm^2$ area of metallographic planes to meet the minimum cracked particle requirements.

To quantify the microstructural damage, the amount of damaged particles can be measured in terms of how much or how many. To answer how much, volume fraction measurements are made using digital image analysis techniques described earlier by

measuring particle areas. From these measurements, how the volume of cracked particles as well as how fraction of the overall volume changes with applied strain and number of fatigue cycles can be shown.

To describe "how many," number per unit area is measured. As mentioned earlier, although three-dimensional number densities cannot theoretically be estimated from random two-dimensional sections, this work considers the two-dimensional number fraction as an adequate approximation, because a similar study of aluminum 6061 alloy loaded in tension along the rolling direction showed good agreement between two-dimensional number fraction and three-dimensional number density [48].

There are numerous ways of quantifying particle size; important descriptors are particle feret maximum diameter and particle area. To measure volume fraction, measurements of particle areas are required. However, for size descriptors, in this work, the particle maximum dimension (maximum feret diameter) is used. Once the particle maximum feret diameters are measured, they can be sorted and placed in different size bins to characterize the size distribution from which the average particle size can be estimated. In addition, one can consider the number of cracked particles in a given size range and divide that by the number of all Fe-rich particles in the same given size range to calculate the probability that a certain size particle will crack at that strain level. It is important to note that the method of scrapping can have a large effect on particle size distributions and average particle size information by significantly changing the number density of particles.

Orientations of cracked and Fe-rich particles have also been measured. The particle orientation may be defined as the angle between the maximum feret diameter and

the horizontal direction. Therefore a particle elongated vertically will have an orientation of 90^{o}. It should be noted that there is a limitation in measuring a smaller particle's orientation due to pixilation effects. Orientation distributions and probabilities can be analyzed in the same way as size distributions using measurements made on each particle's feret orientation. These measurements are useful for characterization of a particles' likelihood of cracking as well as particle rotations.

Finally, to obtain short and long range information about spatial patterns involving cracked and Fe-rich particles, 2-point function correlations and nearest neighbor distributions were estimated using in-house C codes developed by Y. Mao and H. Singh. These spatial descriptors are developed in Chapter II.

CHAPTER IV

RESULTS AND DISCUSSIONS

4.1 Introduction

The objective of this work being to quantitatively characterize the particle cracking damage in Al 7075 as a function of monotonic and cyclic loading conditions, quantitative microstructural measurements were made using both standard and novel digital image analysis techniques on the microstructures of Al 7075-T651 tensile and fatigue type specimens. The experimental data obtained from these measurements on Fe-rich particles are discussed in this chapter. The following section seeks to describe the microstructural damage qualitatively, and that is followed by the quantitative analysis.

4.2 Qualitative Discussion

Figure 1 shows a typical microstructural field of view of the unstrained microstructure of the Al 7075-T651 alloy. Notice, there are two types of particles, namely Mg_2Si (black) and Fe-rich (gray). Also, these particles are aligned in stringers and are elongated and highly directional as a result of hot-rolling. Upon visual inspection, there appears to be a significantly higher amount of Fe-rich particles as

compared to Mg_2Si particles. Figure 12 shows varying gray values distinguishing different Fe-rich particles, suggesting different chemical compositions. Also, Fe-rich particles have larger size(s) than Mg_2Si particles. The particle morphologies are complex and the microstructure is highly heterogeneous.

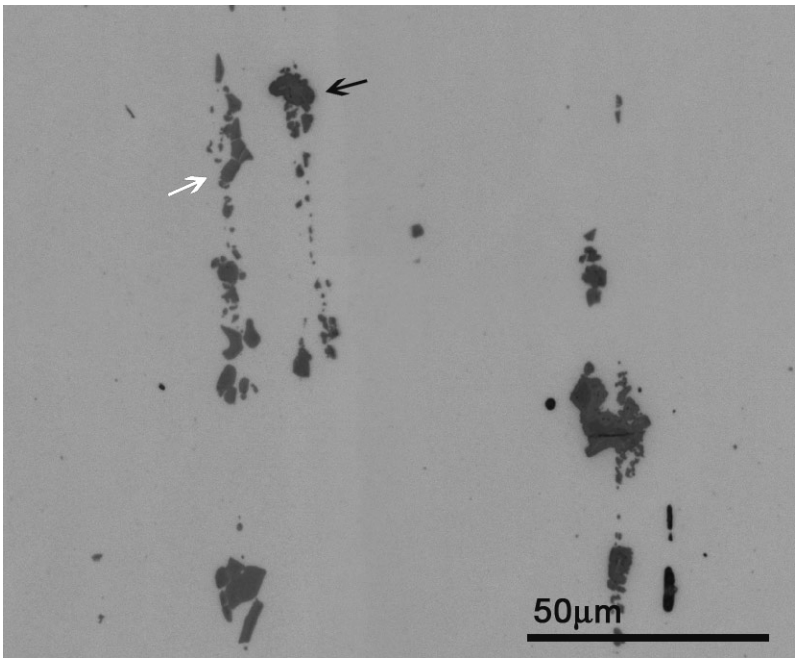

Figure 12 Varying Gray Values Depicting Fe-rich Particles.

Figure 13 shows the microstructure of the failed tensile test Al 7075-T651 specimen. Notice that numerous particles are cracked but not debonded. Also, these cracks appear to be aligned perpendicular to the rolling direction (the direction in which stringers are aligned), which is also the direction of applied stress, and are very thick as a result of the large strain. Due to the darkness of the Mg_2Si particles, it would be nearly impossible to detect cracks in them. Furthermore, generally larger and more elongated particles crack. For these reasons and the fact that Mg_2Si particles are only a small fraction of particles, it has been assumed for this work that the effect of cracking of the Fe-rich particles will much outweigh that of the Mg_2Si particles, and therefore, cracking

of the Mg_2Si is not characterized in this study. It should also be noted that the color of the Mg_2Si particles and the cracks contained within damaged Fe-rich particles have very similar contrast and grayscale values. This leads to difficulties in segmentation of the cracked particles.

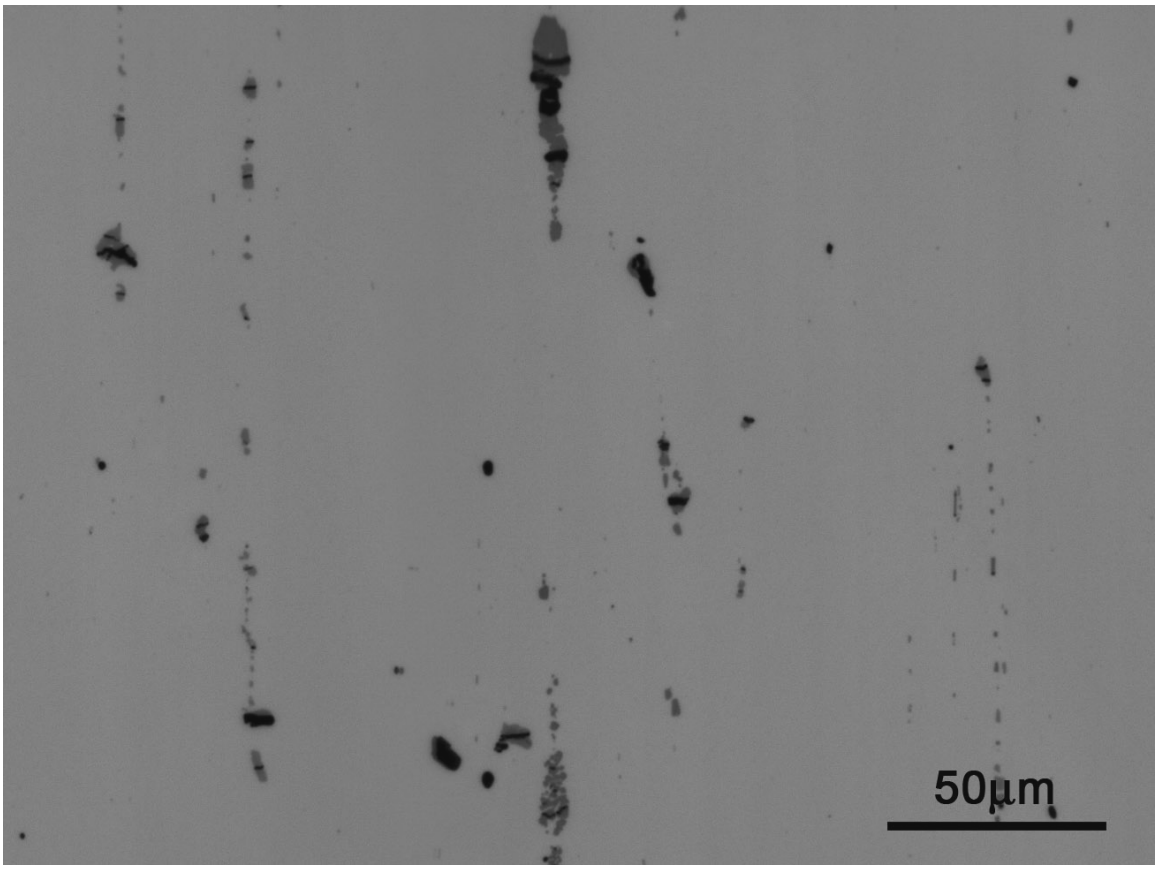

Figure 13 Microstructural Field of a Failed Tensile Specimen.

Figure 14 shows the microstructure of the failed fatigue test specimen Al 7075 alloy fatigue tested at .0075 strain amplitude, and Figure 15 shows the microstructure of the failed Al 7075 alloy fatigue tested at .0025 strain amplitude. Notice less particles are cracked in these fatigue test specimens in comparison to the tensile test specimen (Figure 13). Although the cracks are for the most part also perpendicular to the rolling direction, they are much thinner than cracks in the tensile test specimens.

Finally, from inspection of both tensile test and fatigue test specimens, it seems that larger more elongated particles aligned with the applied stress direction (which is the rolling direction) tend to crack preferentially.

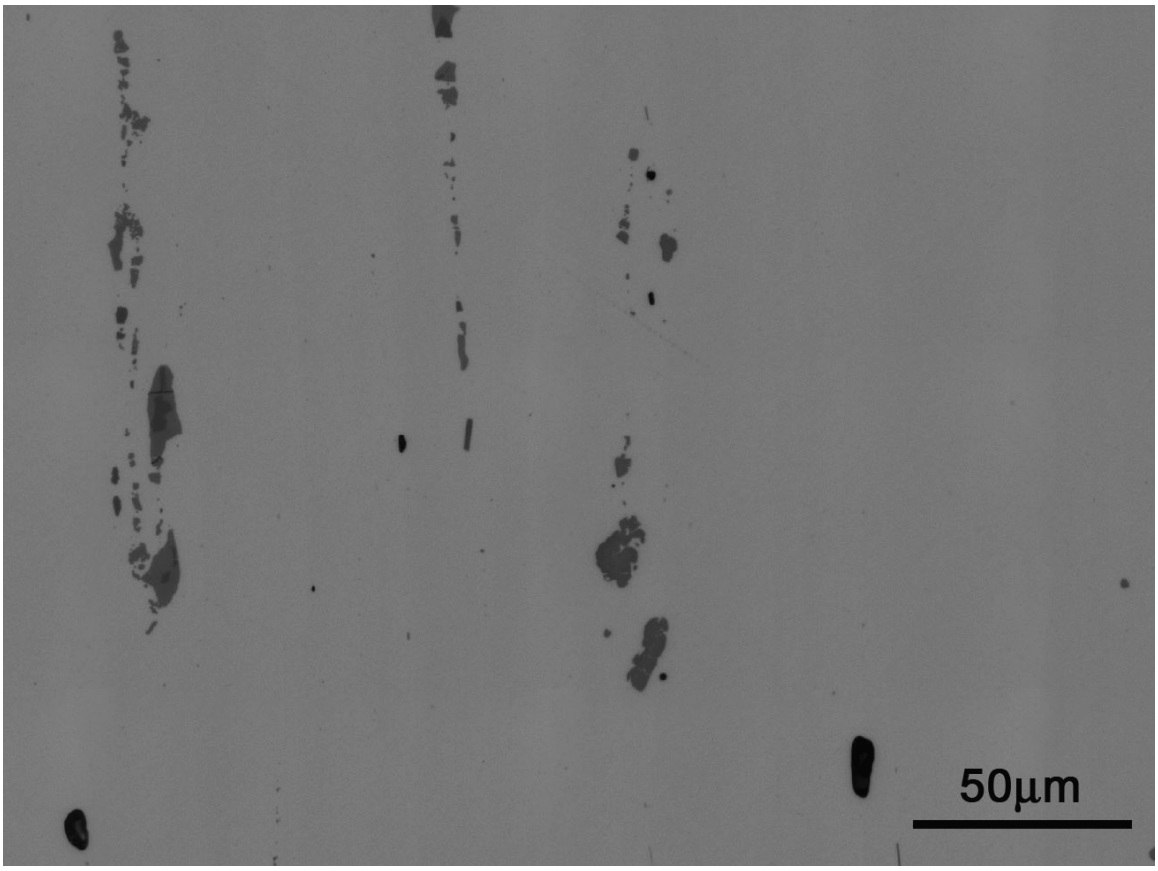

Figure 14 Microstructural Field of a Failed .0075 Strain Amplitude Fatigue Specimen.

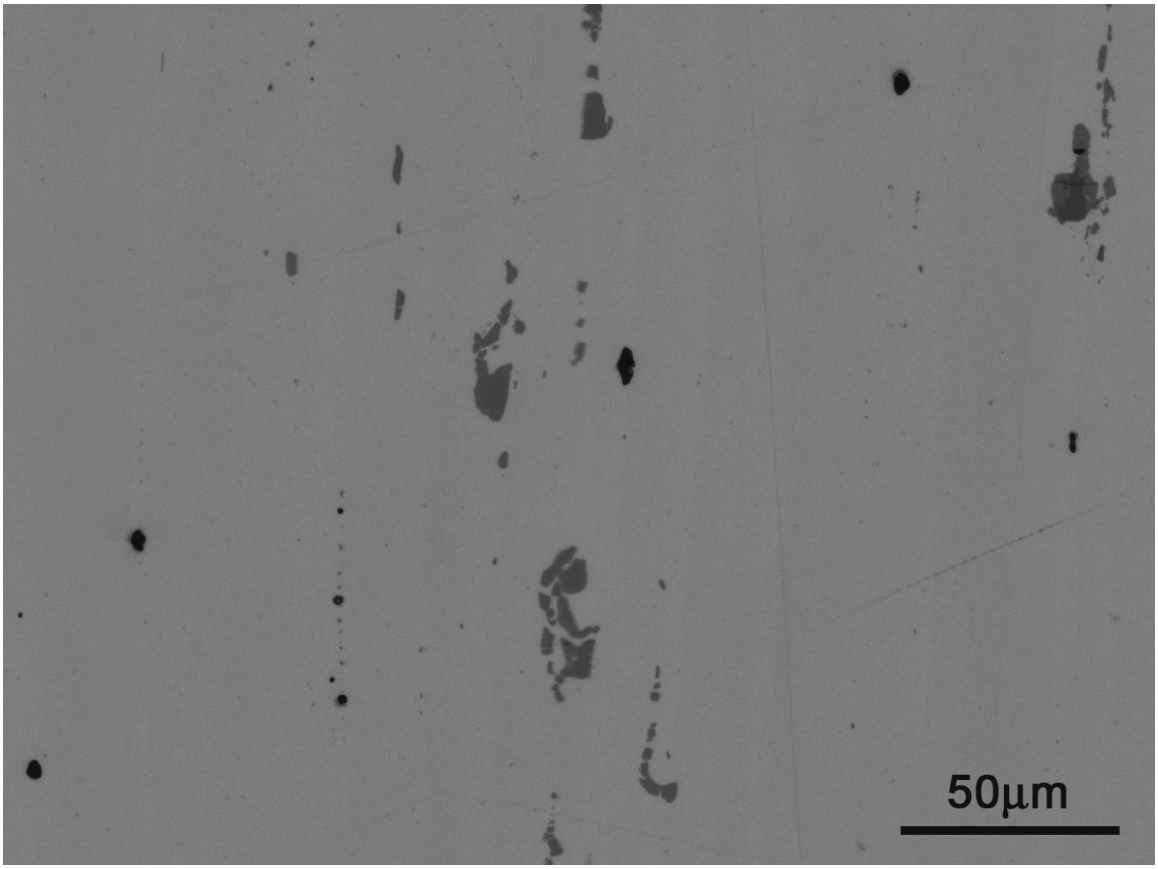

Figure 15 Microstructural Field of a Failed .0025 Strain Amplitude Fatigue Specimen.

4.3 Quantitative Discussion

4.3.1 Particle Volume Fractions

The volume fraction of particles was measured using digital image analysis techniques described earlier for each of the interrupted monotonic and cyclic test specimen. Volume fraction of cracked particles was divided by the volume fraction of all particles to show the percentage of cracked particle volume. Figure 16 shows the relationship between the fractional volume of cracked particles and tensile strain. The trend shows that percentage volume of cracked particles approaches 80% at failure. In

addition, the percentage volume of cracked particles saturates at approximately 10% strain. Figure 17 and 18 show the percentage volume of cracked particles for the cyclic loading conditions, at high strain amplitude (.0075) and low strain amplitude (.0025) respectively. For the cyclic loading condition, the fraction of cracked particle volume is much lower (a maximum of ~18-22%) than that in the monotonic case (~80%). For the failed specimens, the percentage volume of cracked particles is greater for the high strain amplitude fatigue than the low strain amplitude fatigue as one might expect. Also, the damage is comparable at 100 cycles for the high strain amplitude (~14%) and the low strain amplitude (~12%). The low strain amplitude trend seems to settle as early as 1000 cycles whereas the high strain amplitude seems to follow a trend more similar to the strain results with the exception of the data points at 500, 800, 1000 cycles which don't seem to fit the trend. Fatigue is a complicated problem, and it is not the author's intention to completely characterize this process but more so to compare the results with those of monotonic loadings. It seems from these findings that more data are needed to better understand the fatigue damage evolution due to particle cracking.

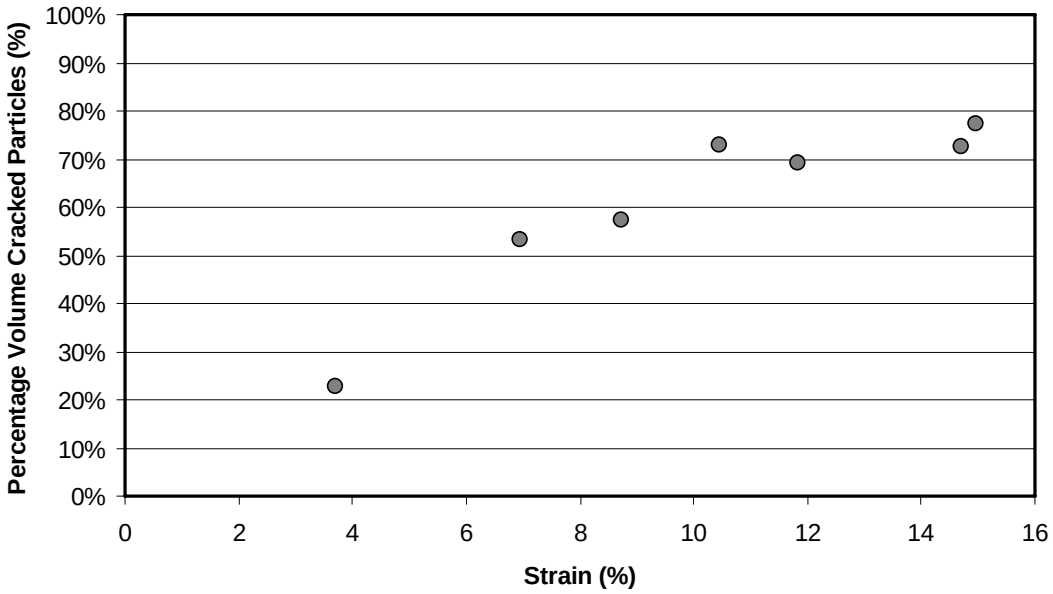

Figure 16 Percentage Volume Cracked Particles (Area) vs. Strain

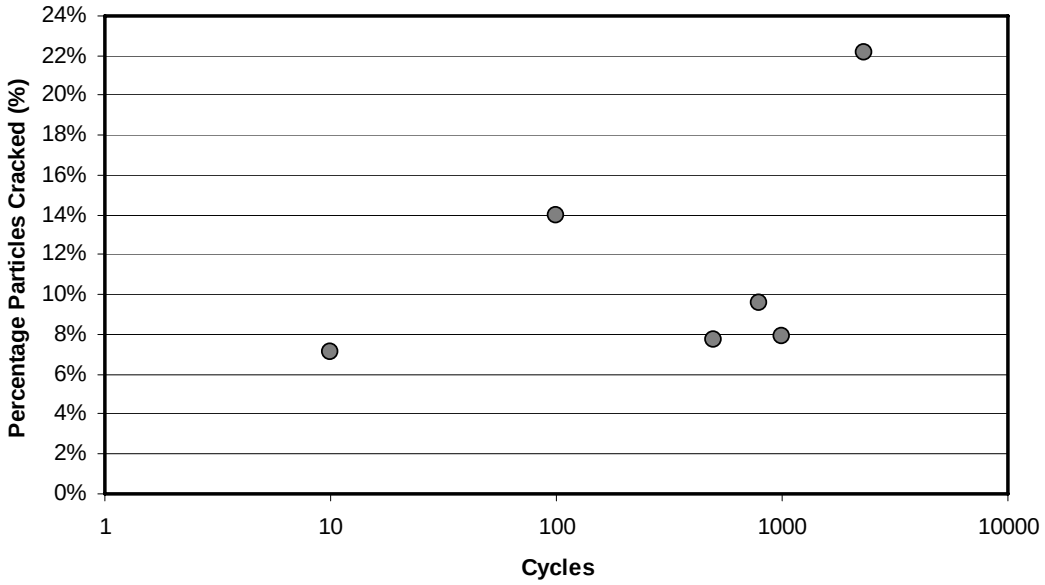

Figure 17 Percentage Volume Cracked Particles (Area) vs. Cycles
for Strain Amplitude .0075

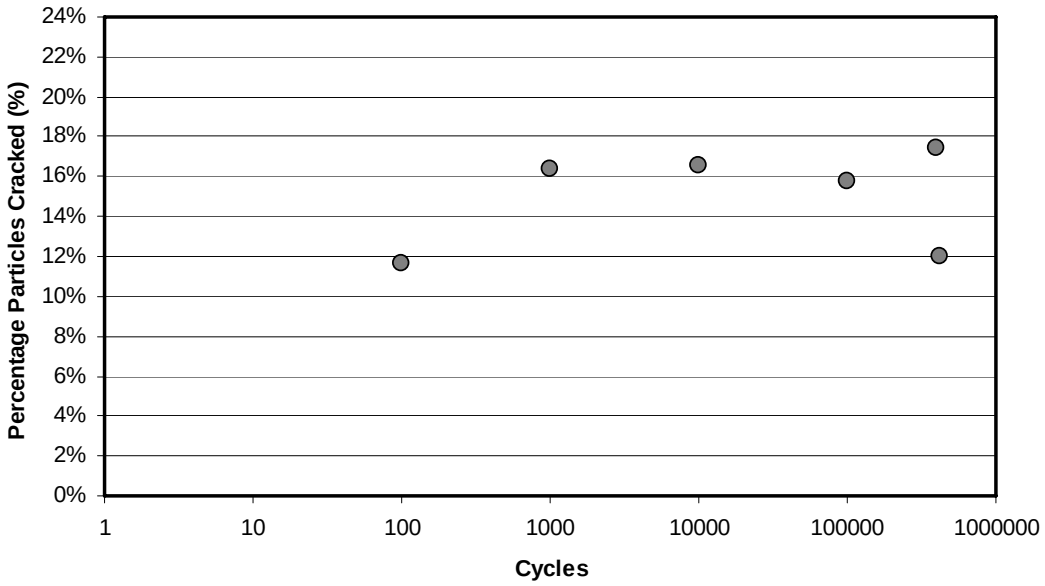

Figure 18 Percentage Volume Cracked Particles (Area) vs. Cycles
for Strain Amplitude .0025

4.3.2 Particle Number Densities

Three-dimensional number density cannot be estimated from random two-dimensional sections. Its estimation requires the use of three-dimensional probes such as the "dissector" technique [46,50-52] or serial sectioning [52-55], both of which are time consuming. However, it has been shown in a previous thesis work by Agarwal [7] that there is a reasonable agreement between three-dimensional number density and two-dimensional number per unit area of cracked Fe-rich particles in a similar alloy loaded in tension along the rolling direction. For this reason, number per unit area (N_A) was extensively measured in this work using digital image analysis techniques described earlier for both monotonic and cyclic conditions. Figure 19 illustrates the relationship between number per unit area (N_A) and tensile strain. To normalize this information for better comparison of different samples, the number fraction is defined to be the number

per unit area of cracked Fe-rich particles divided by the number per unit area of all Fe-rich particles. Figure 20 illustrates how number fraction of cracked particles evolves with applied strain. It is interesting to note that the number fraction has a linear relationship with strain and approaches 45% at failure. This relationship can be represented by the following simple equation:

$$\frac{N_A^{\ C}}{N_A^{\ TOT}} = \frac{(N_A)_0}{N_A^{\ TOT}} + .027e \qquad (4.1)$$

where e is the global engineering tensile strain and $(N_A)_0$ is the number per unit area of cracked particles due to processing, in this case 6.6 /mm^2. For cyclic loading conditions, Figure 21-22 show the relationship between number fraction and the number of cycles for low cycle (.0075) and high cycle (.0025) fatigue specimens, respectively. The trends suggest that the two fatigue regimes have different damage evolution mechanisms. However, several comparisons of figures 20-22 are helpful in describing the number density behavior. First, at 100 cycles, the damage is approximately the same for both low and high cycle. Second, the number fraction is higher at failure for the low cycle as compared to high cycle specimen, which is expected. Third, for the low cycle data at cycles of 500, 800 and 1000, the data seem to be outside the trend. The low cycle trend appears to be more similar to the monotonic results, whereas the high cycle trend tends to saturate at 1000 cycles. And finally, the number fraction stays much lower for both cyclic conditions (approximately 4%) as compared to the monotonic loading (approaches 45%).

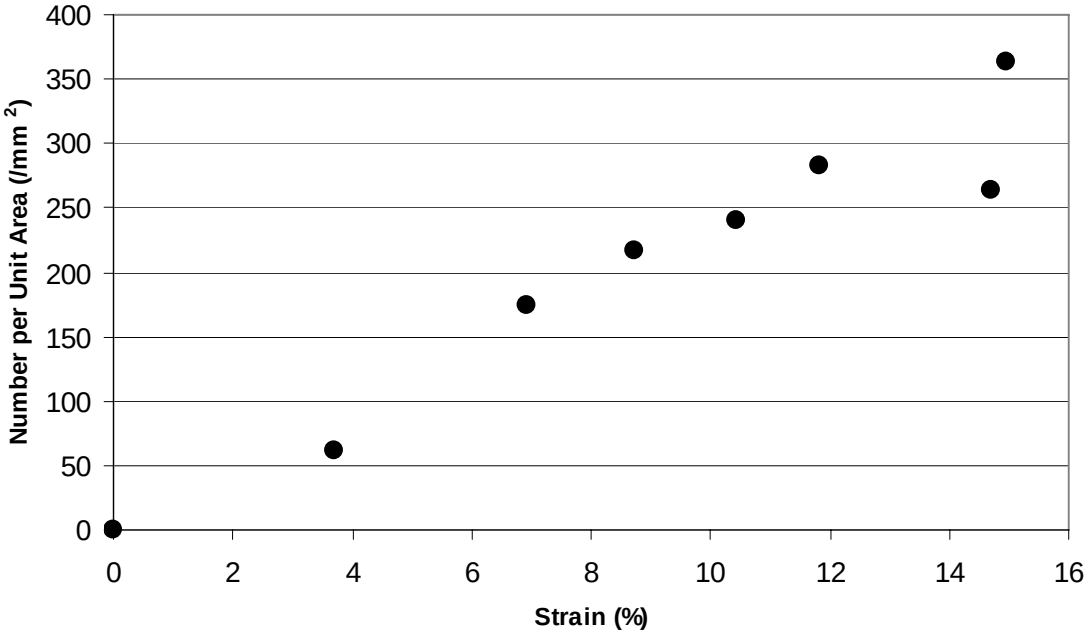

Figure 19 Number per Unit Area Cracked Particles vs. Strain

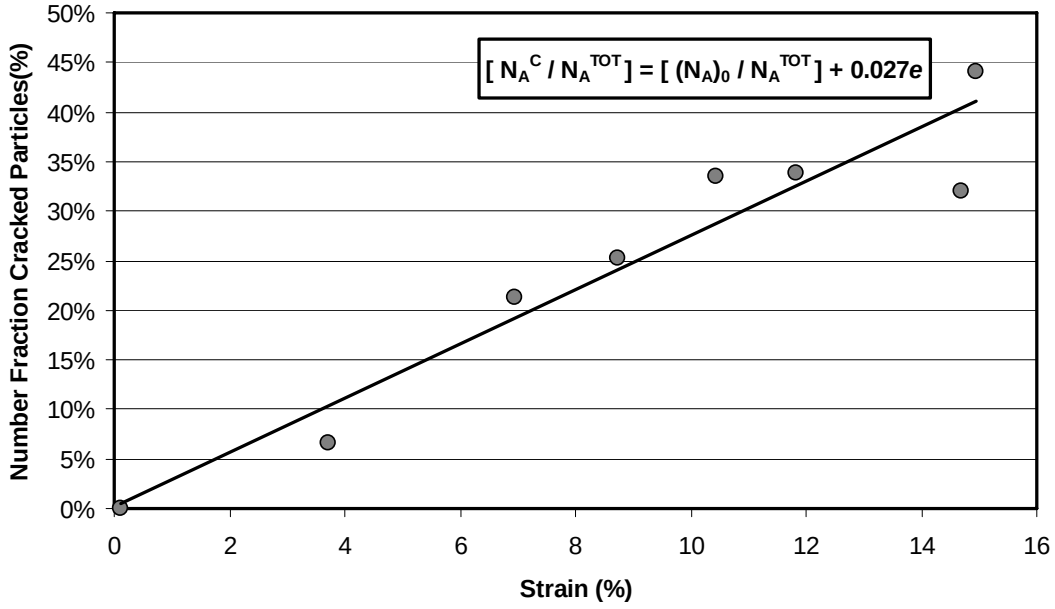

Figure 20 Number Fraction Cracked Particles vs. Strain

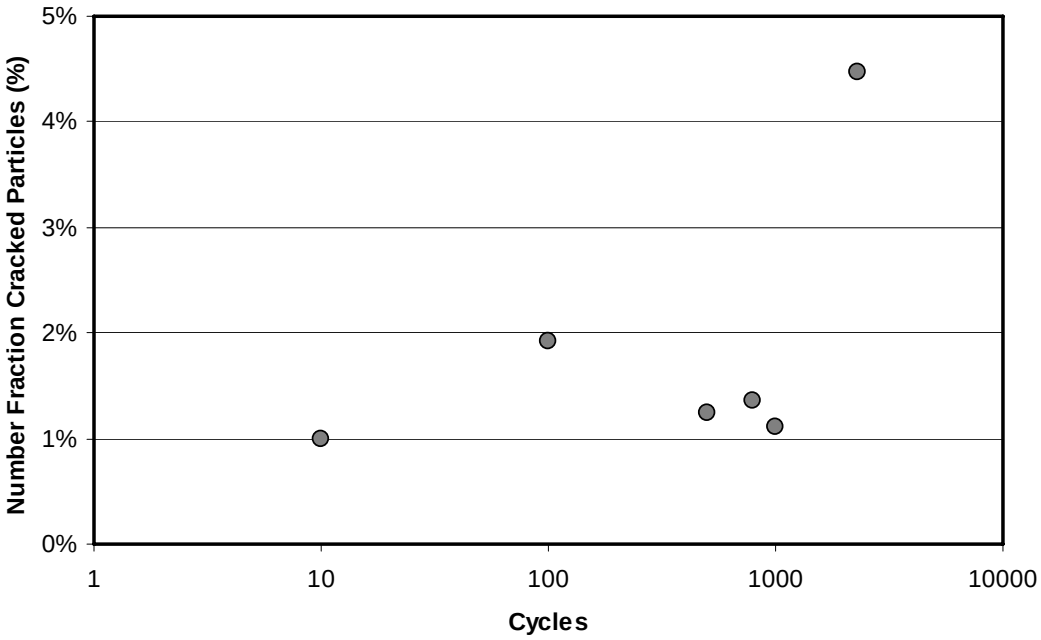

Figure 21 Number Fraction Cracked Particles vs. Cycles
for Strain Amplitude .0075

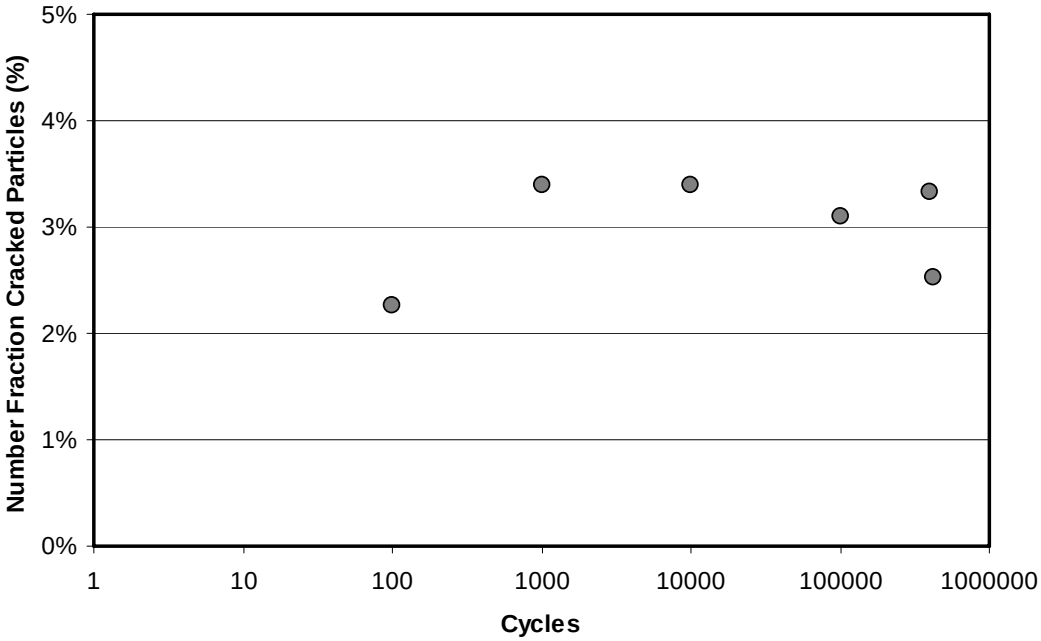

Figure 22 Number Fraction Cracked Particles vs. Cycles
for Strain Amplitude .0025

4.3.3 Particle Average Size

Particle average size can be measured by the maximum feret diameter or by the area. In the present study, the maximum feret diameters were measured using digital image analysis techniques described earlier for both monotonic and cyclic tested samples. Figure 23 illustrates how the average cracked particle size changes as a function of strain. As expected for a robust data set, the average overall Fe-rich particle size varies little from one sample to another (4-5μm). However, the data for average Fe-rich *cracked* particle size shows that, at low strain, the average particle size is 9.5μm and then as strain increases, it decreases and saturates around 8μm. For any applied strain, the average cracked particle size is greater than the global average size of all Fe-rich particles showing that larger particles crack preferentially. Furthermore, the cracked particle size trend suggests that largest particles crack at lower strains, and as strain continues to increase, smaller particles begin crack. This is in good agreement with previous findings that larger particles are more likely to crack due to lower required stresses for fracture. This suggests that larger particles crack at the lower strains, and as strain increases small particles see local stresses high enough to begin cracking. Note that some particle cracking is observed in the unstrained specimens, which essentially represents the damage developed during the hot-rolling process, and therefore, it is not a part of particle cracking damage due to applied stress in these tests. Furthermore, the number of these particles is so small relative to the number that crack after applied strains (~1-10%), that they do not greatly affect the average particle sizes. For the fatigue specimens, Figure 24 and 25 show the high amplitude fatigue and low amplitude fatigue average particle size trends, respectively. When comparing monotonic and cyclic conditions, the average

cracked particle sizes are larger for the cyclic conditions which might be expected because of the lower applied stress levels. However, when comparing the data sets for high and low strain amplitude fatigue specimens, it is perplexing to notice that the high amplitude fatigue has a higher average particle size than the low amplitude fatigue which is contrary to the expectation. One might expect that the higher the strain amplitude the greater number of small particles that will crack resulting in a lower average particle size. However, one explanation is that this effect may be overcome by large particles which are not favorably oriented beginning to crack at the higher strain amplitude. Although average particle size for the high strain amplitude specimens decreases with increased number of cycles, as may be expected, the opposite is found in the low strain amplitude specimens which is also contrary to expectations. This too may be the result of large particles unfavorably oriented beginning to crack. More data needs to be collected to further study the fatigue behavior.

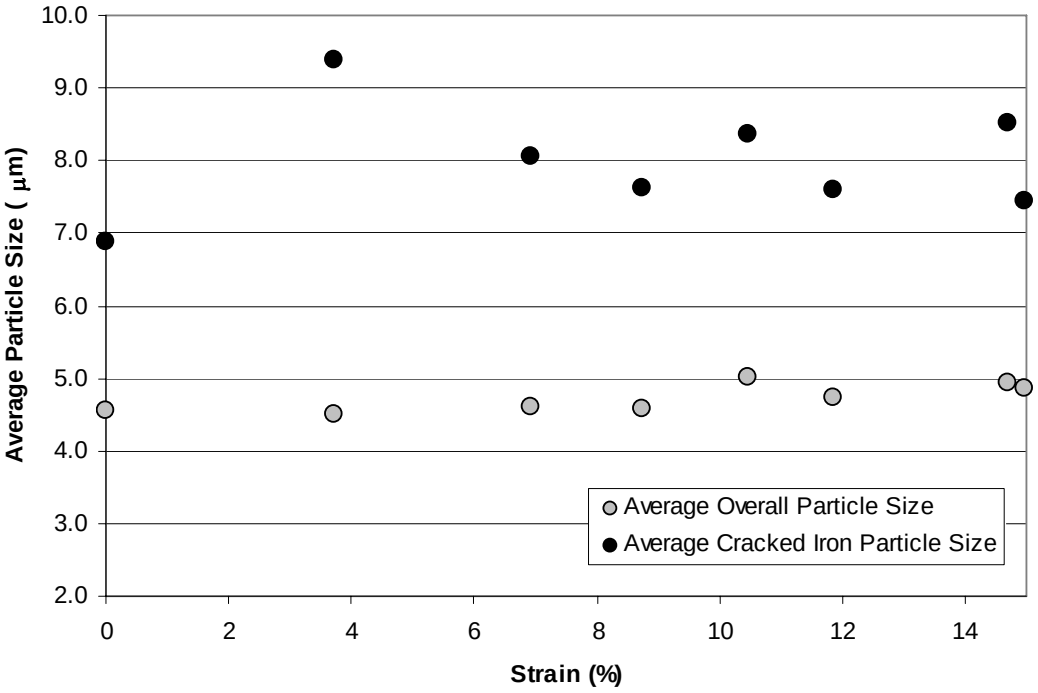

Figure 23 Average Particle Size vs. Strain for Tensile Test Specimens

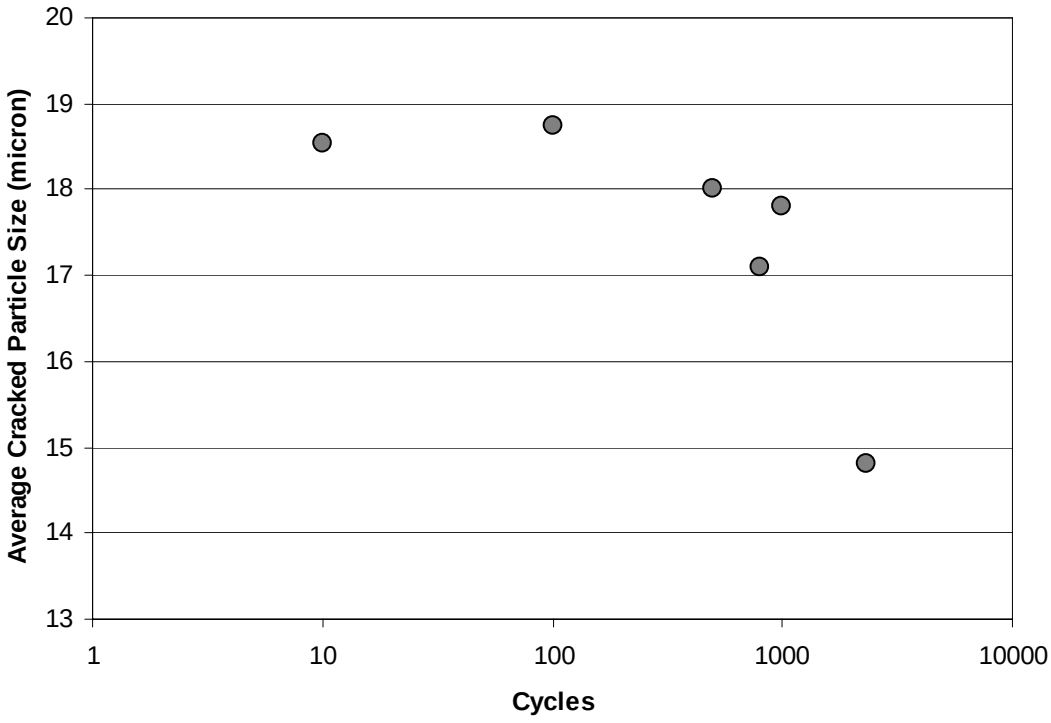

Figure 24 Average Particle Size vs. Cycles for Strain Amplitude .0075

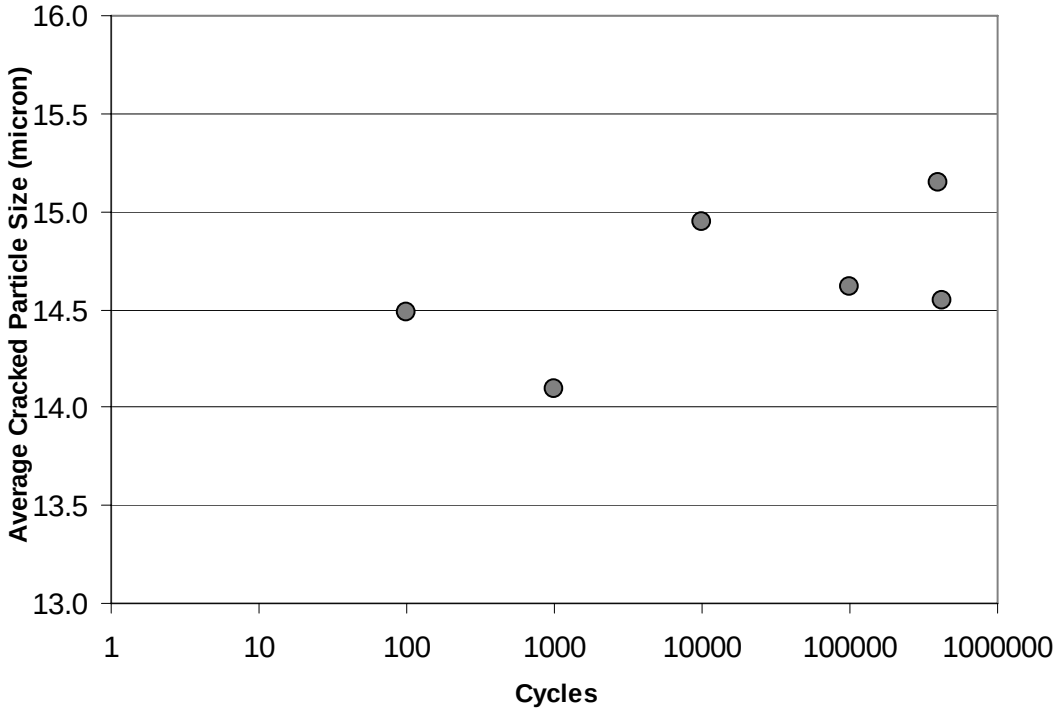

Figure 25 Average Particle Size vs. Cycles for Strain Amplitude .0025

4.3.4 Particle Size Distribution

Particle sizes (maximum feret diameter) were measured using digital image analysis techniques described earlier for each strain level. From these measurements size distributions were computed. Comparison of both cracked and all Fe-rich particle size distributions yields valuable information about cracking behavior. The overall Fe-rich size distribution plot (Figure 26) illustrates that the majority of overall Fe-rich particles are less than 10 μm size. As expected, this average value is the same for different specimens (showing an adequate robust data set). From inspection of the cracked size distribution (Figure 27), the number of cracked particles increases with increasing strain. To compare the Fe-rich overall particle population to the cracked particle population, the size distributions for the 10.45% strained specimen are compared (Figure 28). Inspection

shows that the cracked population appears not to be as heavily skewed as compared to the overall population. To investigate this further, one can normalize each size distribution by its total number of particles. From inspection of the normalized size distribution of the 10.45% strain specimen (Figure 29), it can be seen that larger particles crack preferentially. It is also helpful to consider the likelihood of a particle cracking in a given size range, and for this reason, probability of cracking is developed in the following section.

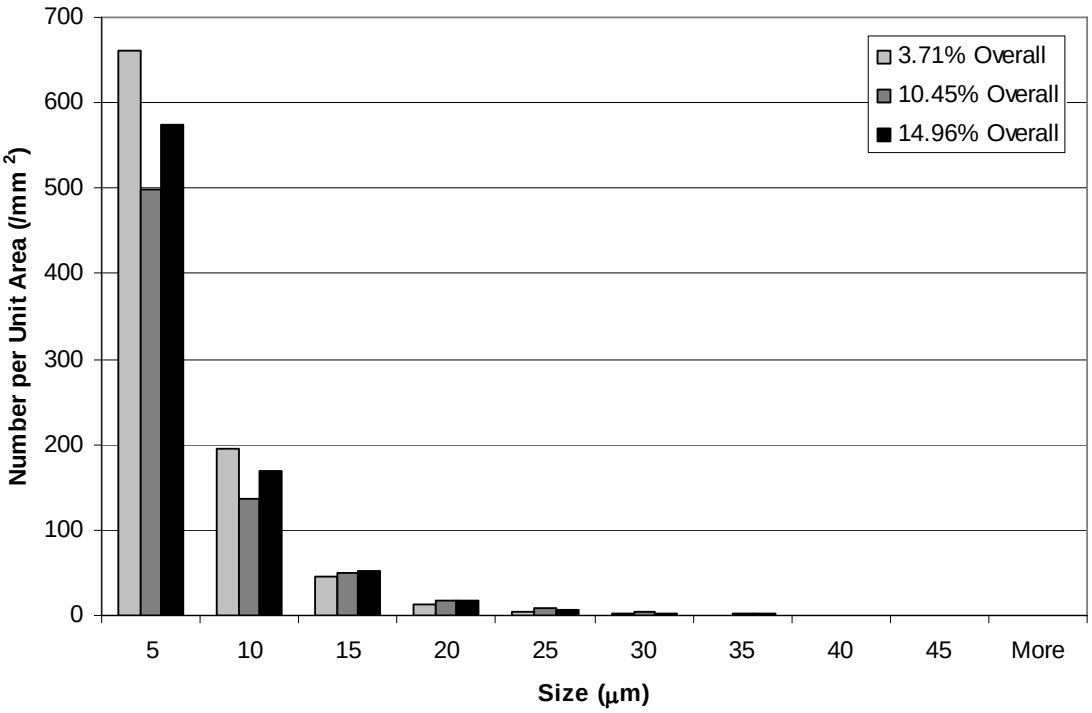

Figure 26 Overall Particle Size Distribution for Tensile Test Specimens

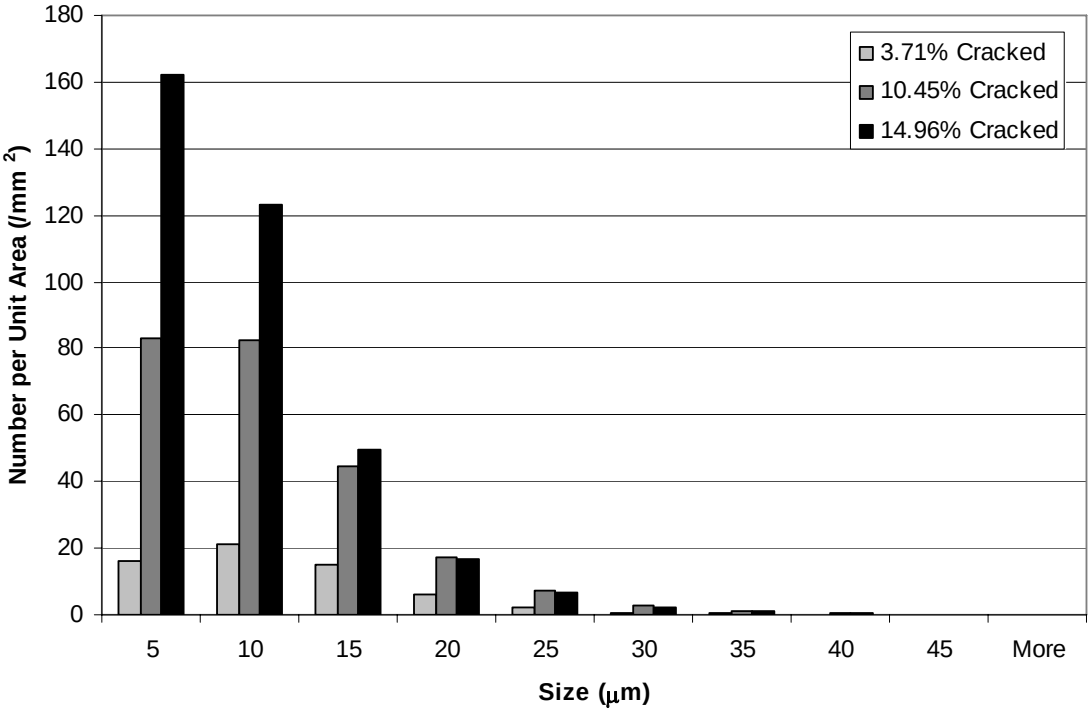

Figure 27 Cracked Particle Size Distribution for Tensile Test Specimens

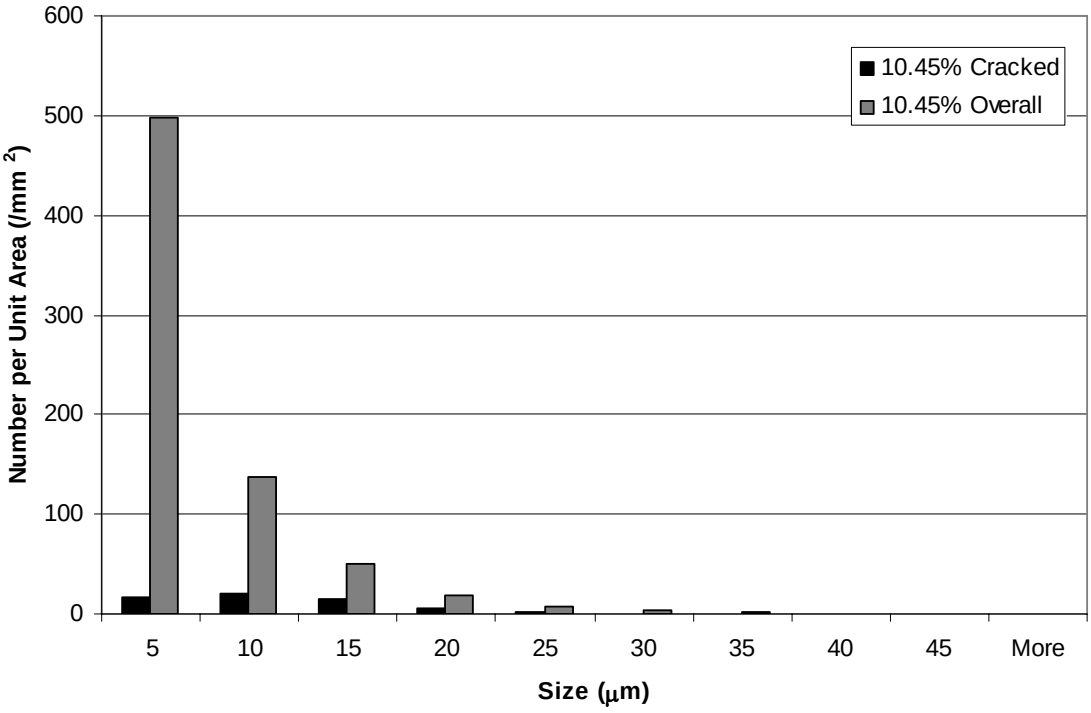

Figure 28 Cracked/Overall Particle Size Distributions for 10.45% Strain Tensile Test Specimen

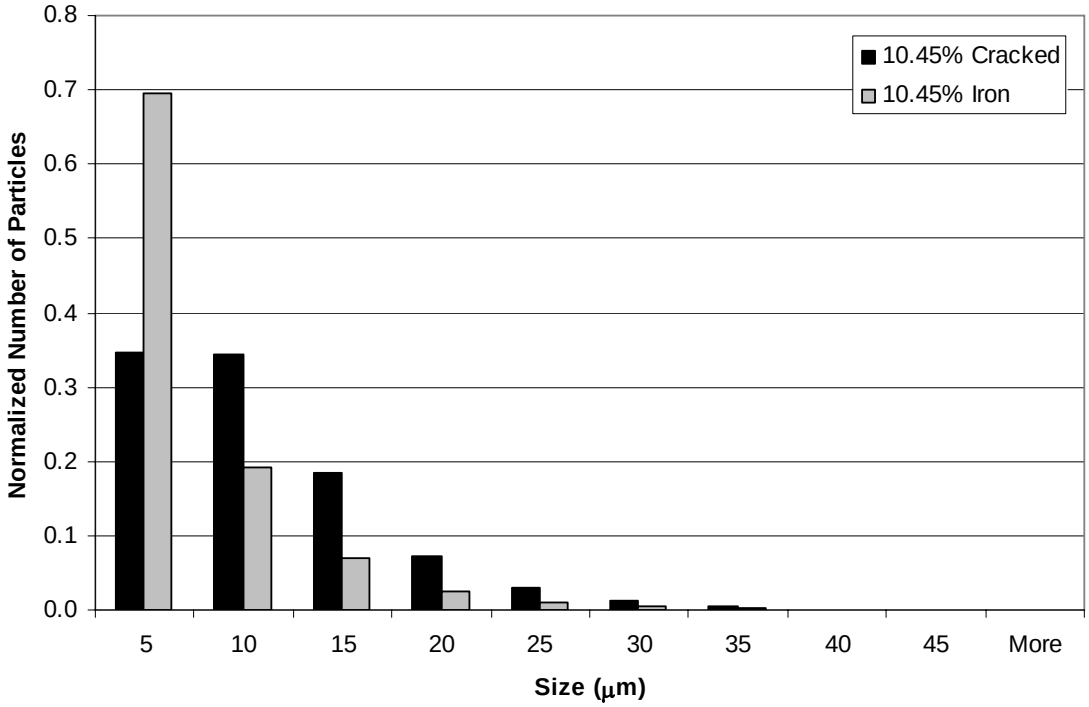

Figure 29 Normalized Cracked/Overall Particle Size Distributions for 10.45% Strain Tensile Test Specimens

4.3.5 Probability of Particle Cracking

The probability of cracking may be defined as the number of cracked Fe-rich particles in a given size range divided by the total number of all Fe-rich particles in the same size range. The probability of cracking can be estimated from the size distribution information. Figure 30 illustrates the probability of cracking for the three strained specimens, pulled to 3.71%, 8.74% and 14.96%. The trend shows that almost all particles larger than 35 μm crack as early as 3.71% strain (25% of failure strain). Furthermore, observe that the specimen strained to 8.74% strain and the specimen strained to failure at 14.96% strain have very similar probabilities of cracking.

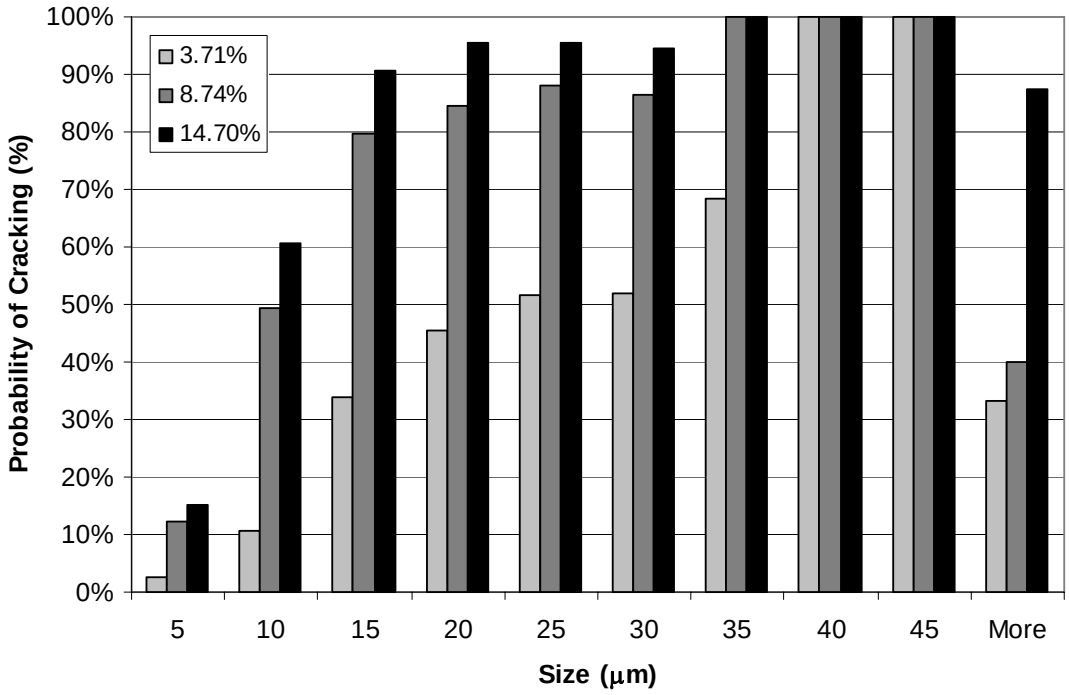

Figure 30 Probability of Particle Cracking Size Distribution for Tensile Test Specimens

4.3.6 Particle Orientation Distribution

In a hot-rolled microstructure, particles are aligned in the rolling direction as well as elongated in that direction due to the hot working process. To quantify damage evolution involving the cracking of constituent particles, it is of interest to determine if particles in one orientation are more likely to crack than others. This was accomplished by measuring the orientation of each particle using digital image analysis techniques described earlier. The angle between the maximum feret diameter and the horizontal axis (direction perpendicular to rolling direction) was measured for this purpose. From these measurements, orientation distributions were computed. Notice from Figure 31 that the majority of particles have orientations within 20^o of the rolling direction or vertical axis (90^o). Figure 32 shows how the *cracked* particle orientation distribution changes as a

function of strain. Notice for each of the three strains the majority of cracked particles also have orientations within 20^o of the rolling direction. Also notice the increase in the number of cracked particles with increasing strain. To compare the number of cracked particles to the number of iron particles, the size distribution is normalized by the number of total particles in the given phase. Therefore, the normalized number of particles in a given range is the number of particles in that range divided by the total number of particles in its overall population. In this manner the orientation distribution of both the cracked and uncracked particles can be compared. From Figure 33 observe that fraction of cracked particles oriented within 20^o of the applied stress direction (rolling direction) is significantly higher than that for overall particle population which demonstrates that particles aligned along applied stress direction are more likely to crack. To better illustrate that there is a preference in cracking for a particular orientation one can consider the probability of cracking.

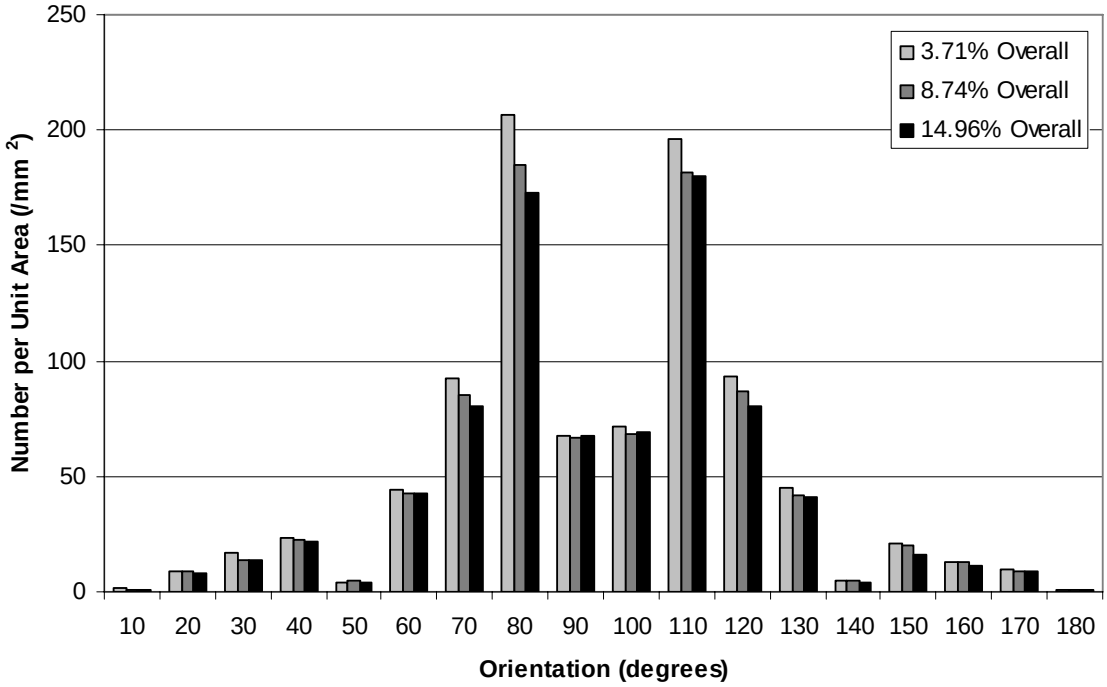

Figure 31 Overall Fe-rich Particle Orientation Distributions for Tensile Test Specimens

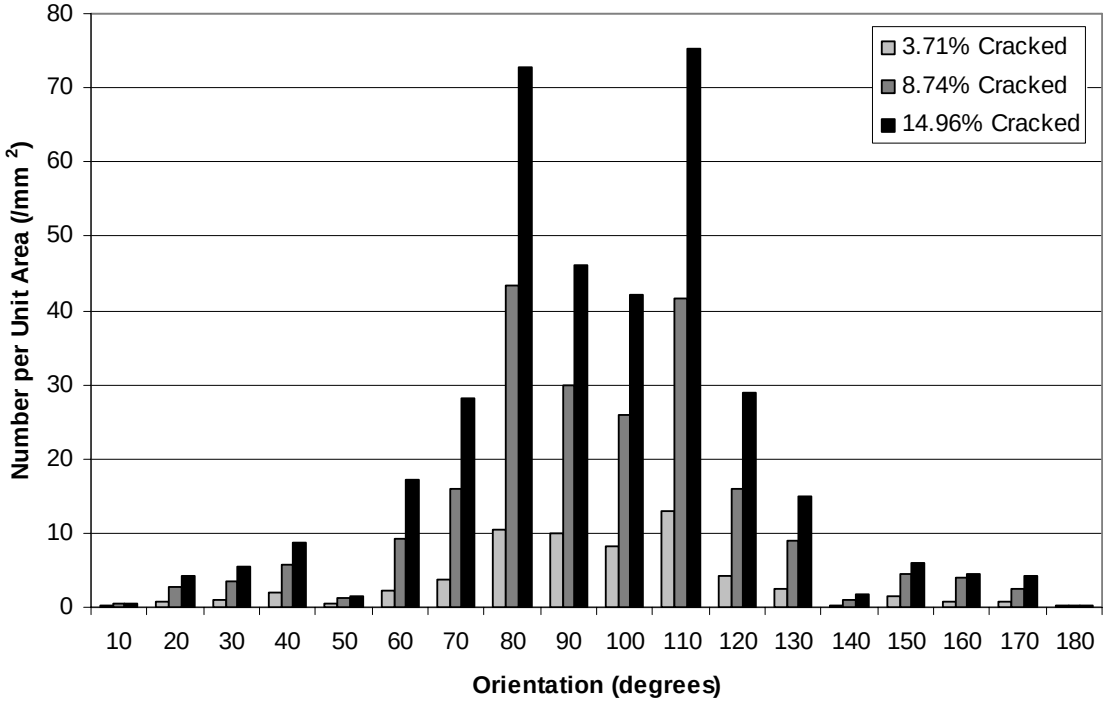

Figure 32 Cracked Fe-rich Particle Orientation Distributions for Tensile Test Specimens

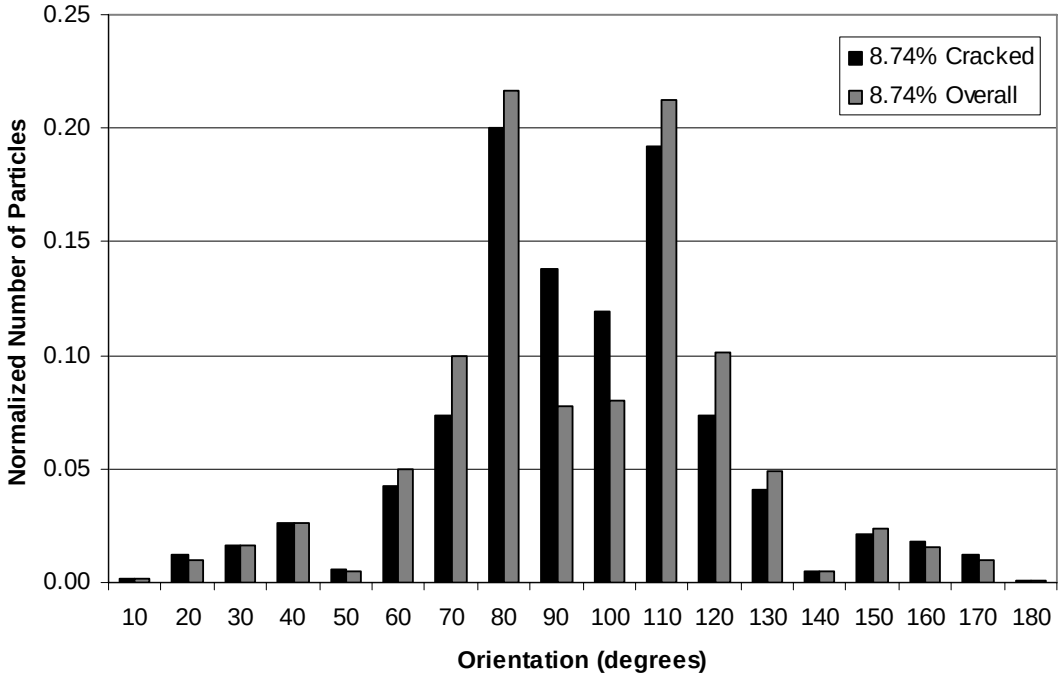

Figure 33 Normalized Orientation Distribution for 8.74% Strain Tensile Test Specimen

4.3.7 Effect of Orientation on Probability of Cracking

The probability of cracking may be defined as the number of cracked particles in a given orientation range divided by the total number of particles in that orientation range. The distribution of probability of cracking (Figure 34) shows that for each of three strains (3.71, 8.74, 14.96%) the particles within 10^{o} of the rolling direction are more likely to crack than other orientations. Furthermore, there is little variation in the probability of cracking for other orientations at a given strain level. From this distribution, one should also notice the similarity between the 8.74 and 14.96% strain levels which is in good agreement with results of cracked particle number densities and cracked volume fractions.

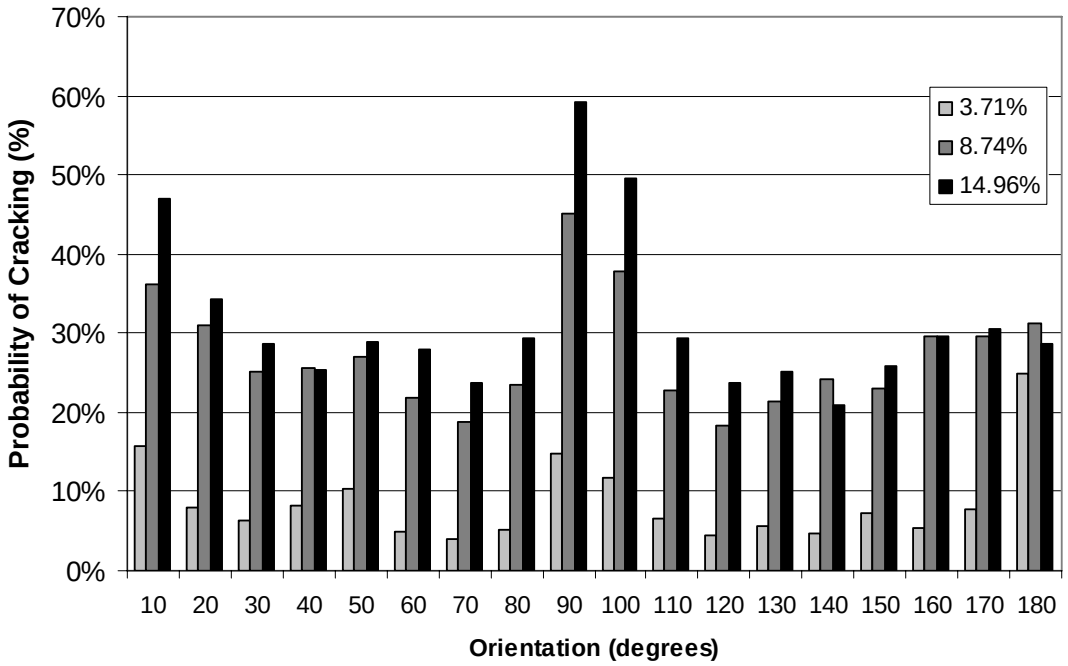

Figure 34 Probability of Cracking Orientation Distribution for Tensile Test Specimens

4.3.8 First Nearest Neighbor Distribution

Nearest neighbor distance (NND) information for Fe-rich particles can be plotted several different ways. For the purpose of comparing damaged particles and the overall particle population, only the overall-overall and cracked-cracked nearest neighbor distributions were considered. As expected, the nearest neighbor distances of iron-iron particles are much less than those of cracked-cracked particles due partly to the large difference in number density in each particle population. This is illustrated by Figure 35, where the nearest neighbor distance decreases from 170μm (damage due to processing) to 16μm (as compared to the 10μm nearest neighbor distance for the overall population). Figure 36 shows the percentage of NND (number in a size bin divided by number in all size bins) in the cracked-cracked nearest neighbor distribution for each of three strains

(3.71%, 10.45%, 14.96%) to illustrate how the distribution evolves with strain. As one would expect, the increase in strain increases the number of particles that crack and thus shifts the nearest neighbor distribution towards the smaller nearest neighbor distance ranges. However, notice that for all strains the majority of nearest neighbor distances is within 0-10μm. Figure 37 compares the overall-overall nearest neighbor distribution to the cracked-cracked nearest neighbor distribution by also normalizing to the percentage of NND. As one would expect, this plot illustrates that the cracked particles are less likely to have nearest neighbor in the 0-10μm range and more like to have nearest neighbors in the 10μm and greater ranges. However, to investigate whether this is only a result of the increased total number of particles, these distributions can be normalized by the square root of the number per unit area. Figures 38-39 show the results of this normalization. These normalized nearest neighbor distributions (NND) are approximately the same at different strain levels. Therefore, the change in the NNDs with strain are primarily due the increase in the number density of cracked particles and not due to change in the intrinsic clustering tendency. This relationship is beneficial for damage modeling because one only needs to measure a single nearest neighbor distribution and the number per unit areas to compute the full range of nearest neighbor distributions.

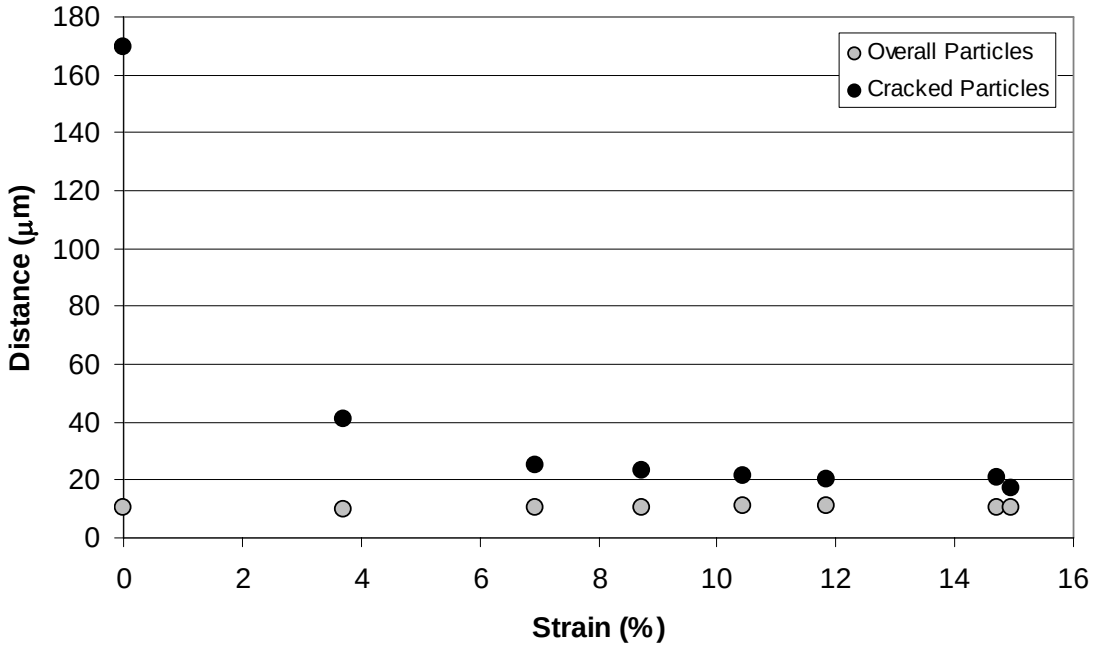

Figure 35 Average First Nearest Neighbor Distances vs. Strain for Tensile Test Specimens

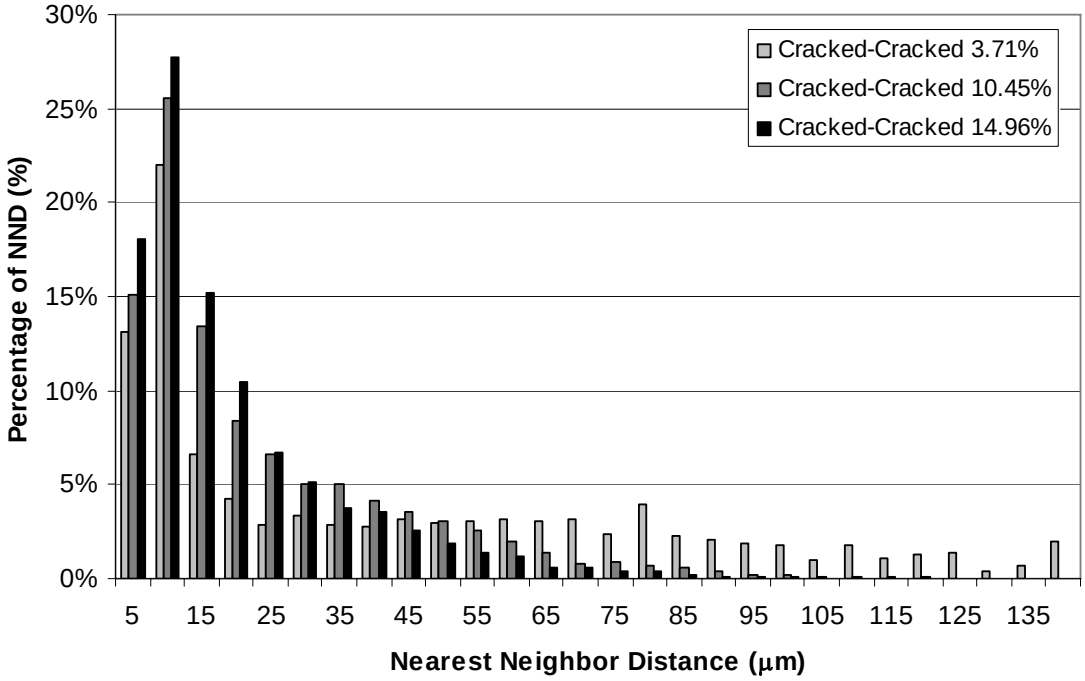

Figure 36 Cracked Normalized Nearest Neighbor Distribution for Tensile Test Specimens

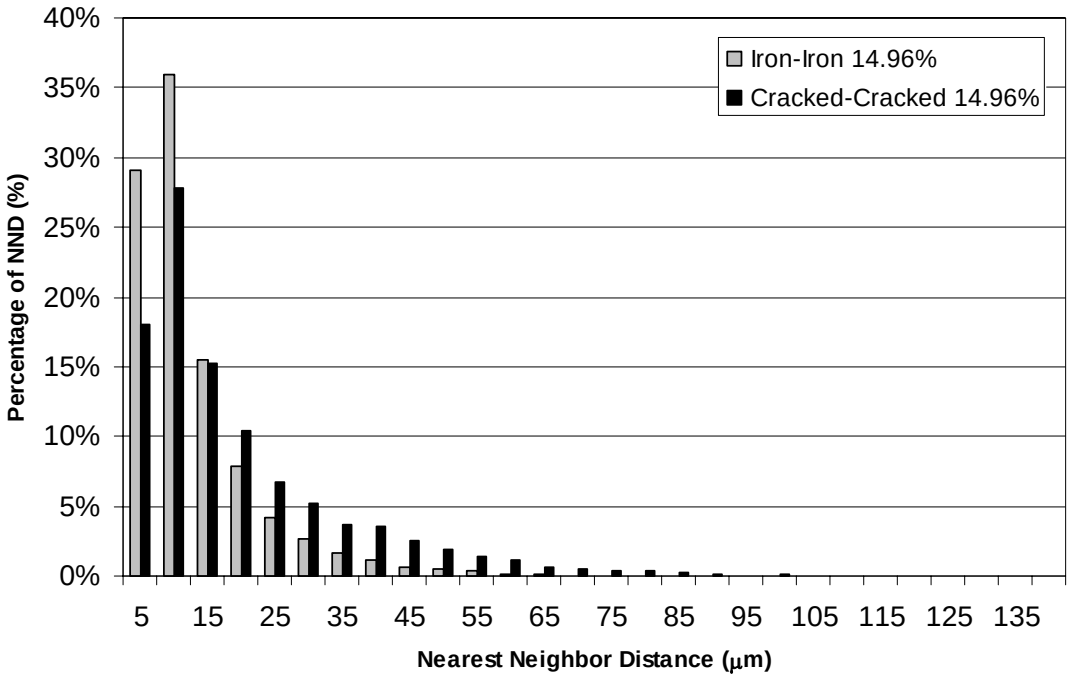

Figure 37 Nearest Neighbor Distribution Comparison
for Tensile Test Specimens

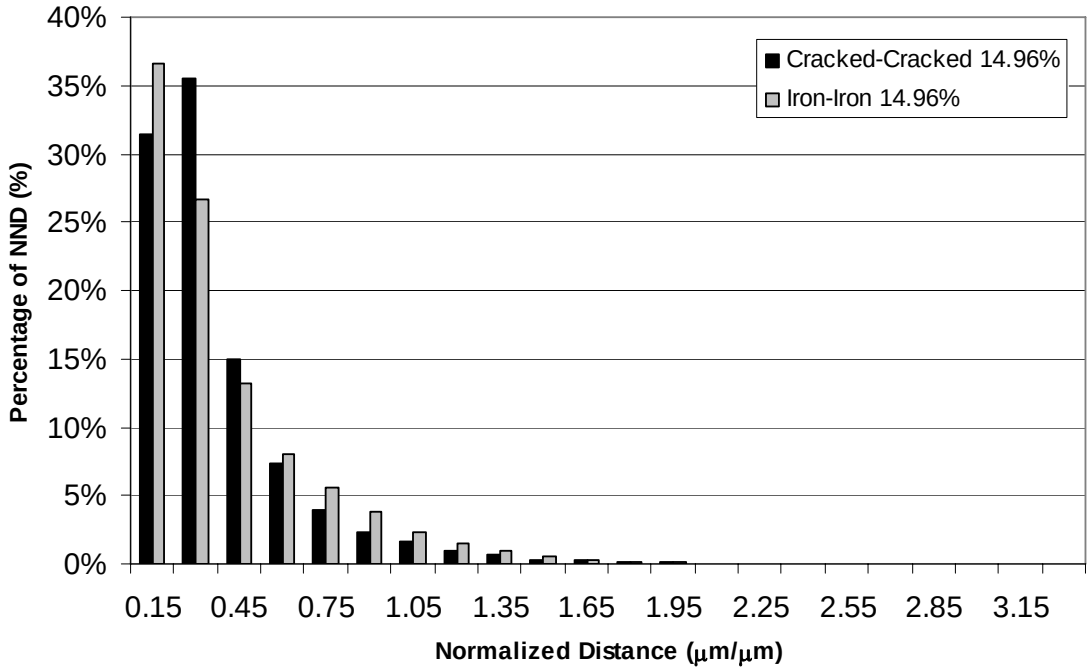

Figure 38 Distance Normalized Nearest Neighbor Distributions Comparison
for Tensile Test Specimens

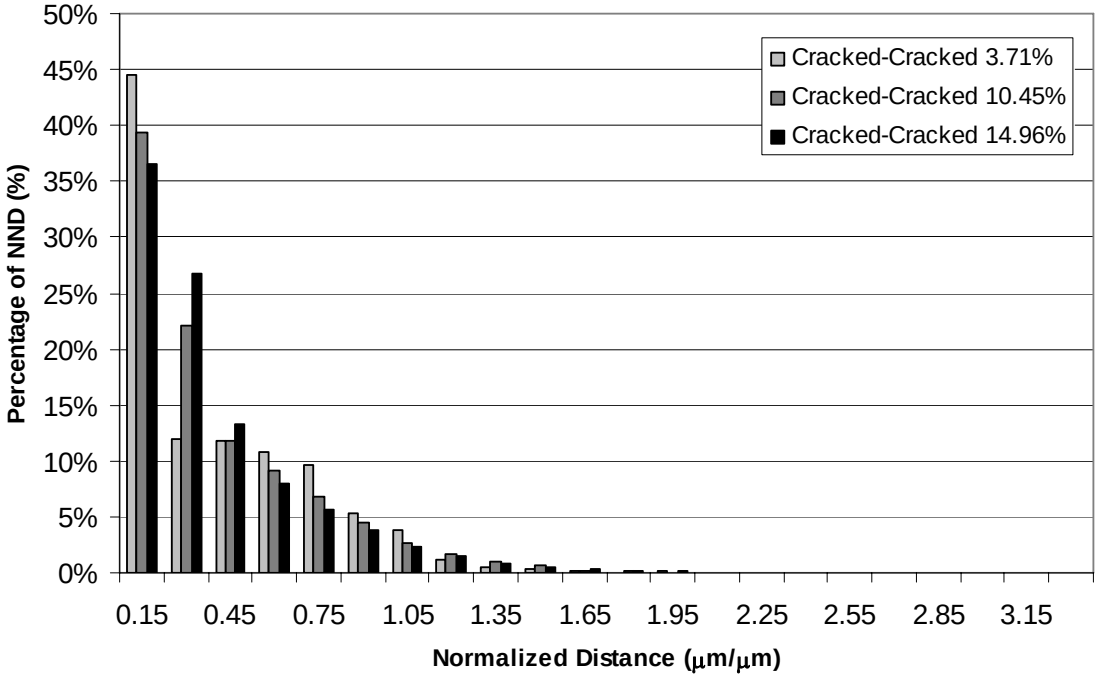

Figure 39 Distance Normalized Cracked Nearest Neighbor Distributions for Tensile Test Specimens

4.3.9 2-Point Function

The 2-point correlation functions for both the rolling and thickness directions for the cracked population and overall population were measured using in house computer codes and are given in Figures 40-43. As one would expect for a hot-rolled microstructure, inspection of Figures 42-43, show that the 2-point function of iron stabilizes much more quickly for the thickness direction than the rolling direction, meaning the particles are both aligned in the rolling direction and having high aspect ratios. It is interesting to note that this trend is also apparent in the cracked particle population as well (Figures 40-41). Comparisons between cracked and iron particles are hard to make using the 2-point correlation function because the microstructures have largely different characteristics such as particle size and volume fraction. However, the

most important utility of the 2-point correlation functions for this microstructure are that they could be used for microstructural modeling and simulations. Due to the enormous amount of time required to gather such information, microstructural simulation would be more efficient way of studying and designing such a material. Such modeling has been done for the overall population by Y. Mao [56] and modeling for other materials has been done by Y. Singh [57,58].

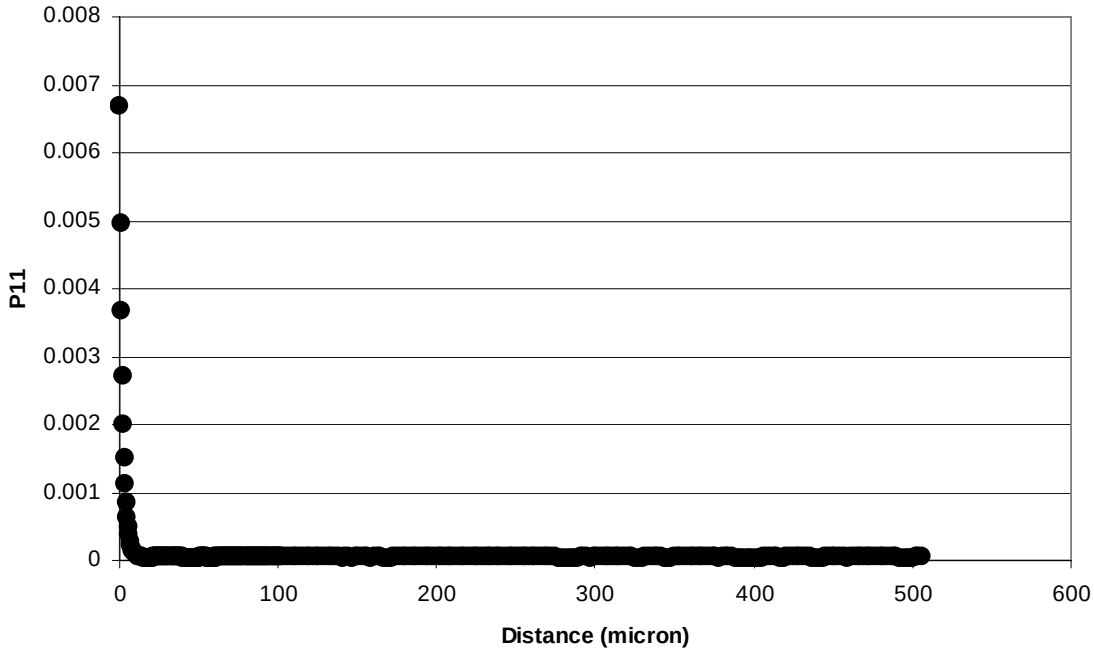

Figure 40 Cracked-Cracked Two Point Correlation Function P11 Thickness Direction for 14.96% Tensile Specimen

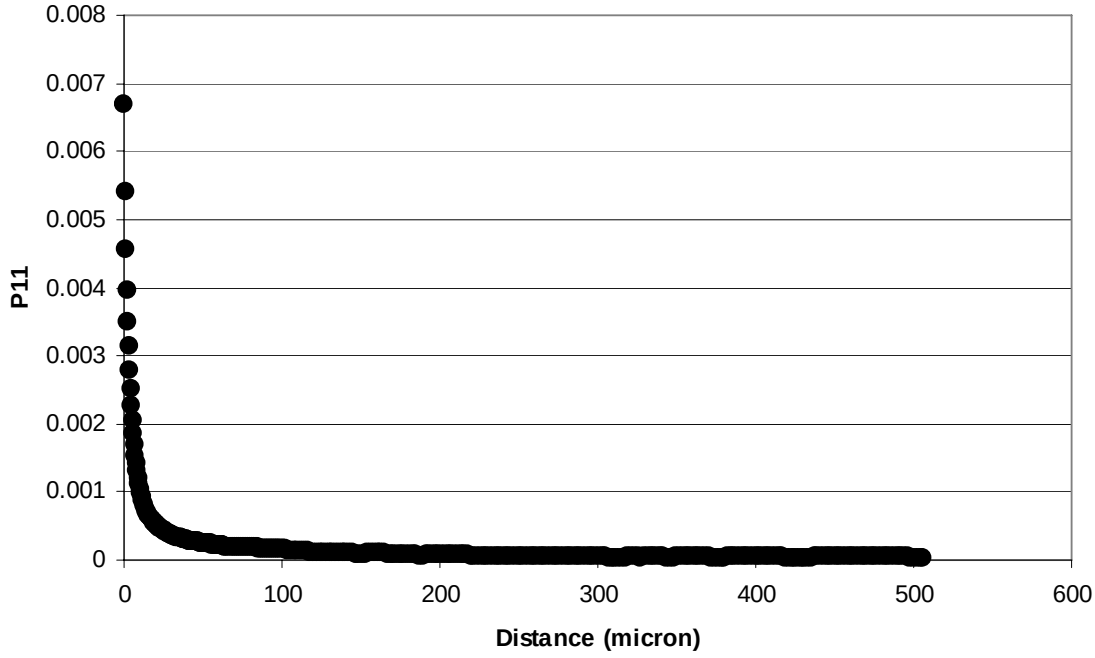

Figure 41 Cracked-Cracked Two Point Correlation Function P11
Rolling Direction for 14.96% Tensile Specimen

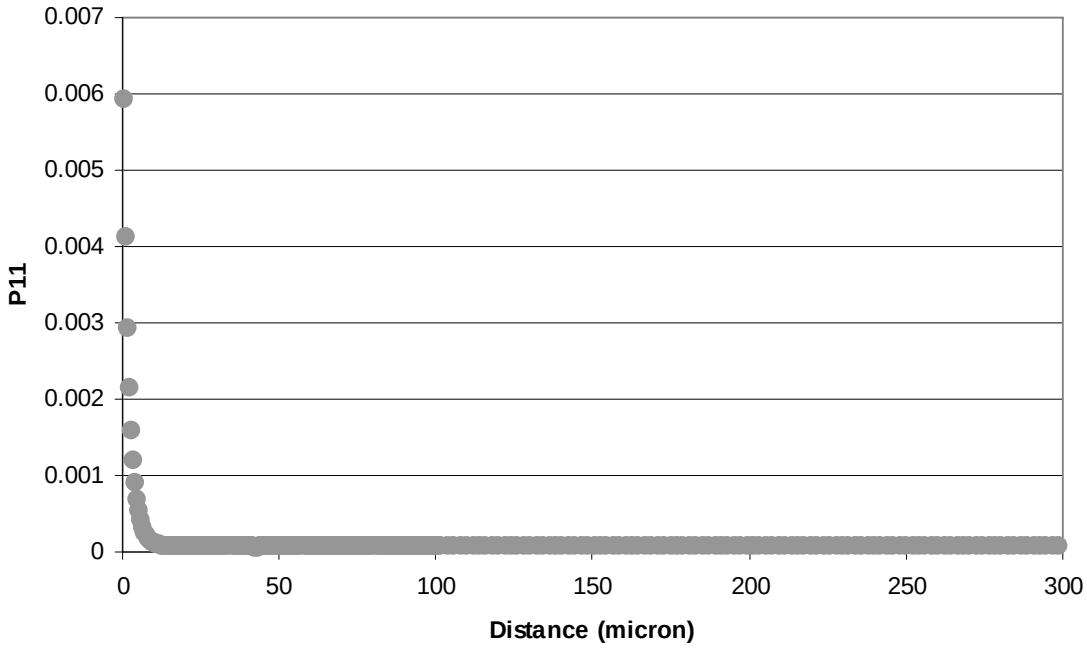

Figure 42 Iron-Iron Two Point Correlation Function P11
Thickness Direction for 14.96% Tensile Test Specimen

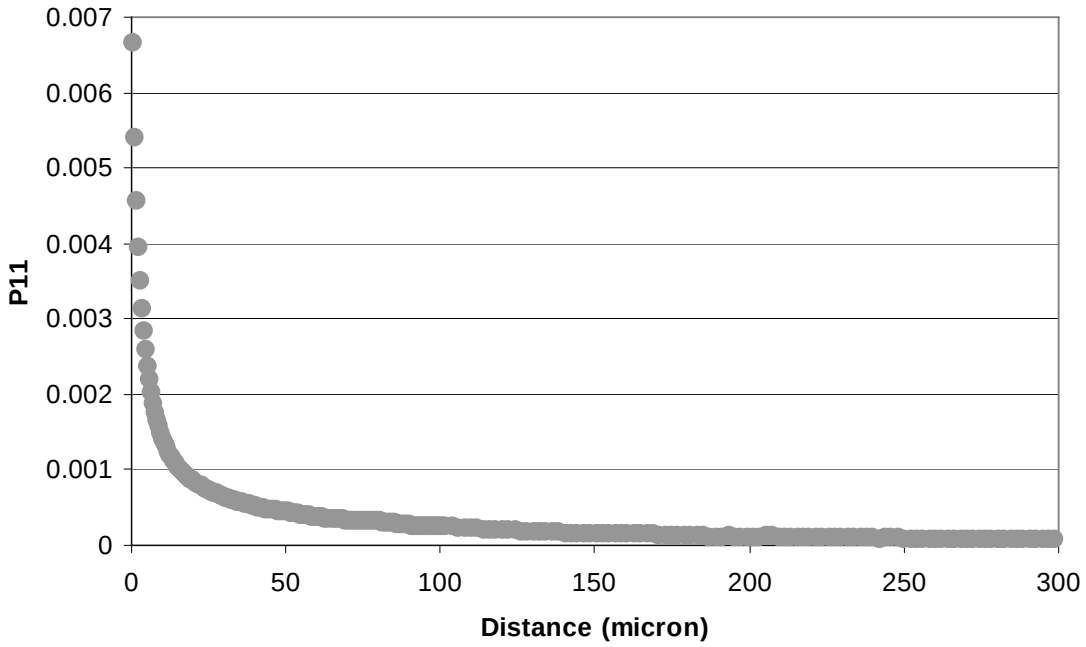

Figure 43 Iron-Iron Two Point Correlation Function P11
Rolling Direction for 14.96% Tensile Test Specimen

CHAPTER V

SUMMARY AND CONLUSIONS

Particle cracking damage in 7xxx series Al-Zn-Mg-Cu-base wrought Al-alloy is quantitatively characterized as a function of strain under uniaxial tension and as a function of number of cycles under low cycle fatigue and high cycle fatigue conditions. The number density, volume fractions, sizes and orientation distributions, two-point correlation functions, and nearest neighbor distributions of damaged Fe-rich particles as well as overall particle population are experimentally measured using stereological and digital image analysis techniques. The quantitative microstructural data lead to the following observations and conclusions:

- Under the monotonic uniaxial tensile loading condition, cracking of Fe-rich constituent particles increases linearly with applied strain which is attractive for damage modeling. The number fraction of cracked particles approaches 50% at failure, and the fraction of cracked particle volume approaches 80% at failure.
- Under all loading conditions studied, larger particles crack preferentially. For the monotonic case, as strain increases, some smaller particles also crack as local strains or stresses increase. Therefore, adapting the processing to reduce the number of the largest particles may favorably change the fracture related properties.

- For high cycle and low cycle fatigue conditions, the number fraction of cracked particles stays much lower than that under uniaxial tensile stress loading and varies less with number of fatigue cycles, and therefore, fatigue fracture should involve highly localized damage.
- For the cyclic loading, an approximate linear increase in number and volume of cracked particles is followed at the high strain amplitude, whereas the number and volume of cracked particles saturates for the low strain amplitude. This suggests that the damage processes of the two regimes are different.
- For the monotonic case, almost all particles with sizes greater than 35μm crack as early as 3.71% strain. Larger particles have higher probabilities of cracking at all strains. At strains larger than 8.74%, probabilities of particle cracking reach saturation levels which is attractive for damage modeling.
- For the monotonic case, particles with orientations within 20^{o} of the applied stress direction have the largest probability of cracking, and therefore larger particles favorably oriented with the applied stress direction are most likely to crack.
- For the monotonic case, nearest neighbor distributions appropriately normalized by the square root of the number per unit area for both iron and cracked particles are independent of strain. This means that these nearest neighbor distributions are primarily dependent on the number density of particles and that the clustering tendency does not change with different applied strains. Therefore, information from only one strain level essentially captures the behavior due to spatial arrangements at all strain levels provided number density of cracked particles is known.

- Further studies need to be done to characterize the particle cracking during fatigue to better understand damage nucleation due to particle cracking.

REFERENCES

[1] W. F. Smith, Structure and Properties of Engineering Alloys, McGraw-Hill, New York, NY, 1981.

[2] K.M. Gruenberg, B.A. Craig, and B.M. Hillberry, “Probabilistic method for predicting the variability in fatigue behavior of 7075-T6 aluminum,” AIAA Journal, vol 37, no10, 1999, 1304.

[3] A.P. Boag, D.G. McCulloch, D.N. Jamieson, S.M. Hearne, A.E. Hughes, C.G. Ryan, S.K. Toh, “Combined nuclear microprobe and TEM study of corrosion pit nucleation by intermetallics in aerospace aluminum alloys,” Nuclear Instruments and Methods in Physics Reearch, b231, 2005, 457-462.

[4] G.T. Hahn and A.R. Rosenfield, Metall. Trans. A, 1975, vol. 6A, pp. 653-70.

[5] S.P. Rawal and J. Gurland, Metall. Trans. A, 1977, vol. 8A, pp. 691-98

[6] E.A. Starke, Jr., Mater. Sci. Eng., 1977, vol. 29, pp. 99-115.

[7] J. Gurland and J. Plateau, “The mechanism of ductile fracture in metals containing inclusions,” Trans. ASM, Vol. 56, PP 442-452, 1963.

[8] F. A. McClintock, “On the mechanics of fracture from inclusions,” Ductility, Metals Park, Ohio, 1968.

[9] M. F. Horstemeyer and A.M. Gokhale, “A void-crack nucleation model for ductile metals,” International Journal of Solids and Structures, Vol. 36, PP 5029-5055, 1999.

[10] M. F. Horstemeyer, J. Lathrop, A.M. Gokhale, and M.D. Dighe, “Modeling stress state dependent damage evolution in a cast Al-Si-Mg aluminum alloy,” Theoretical and Applied Fracture Mechanics, Vol. 33, PP 31-47, 2000.

[11] M. F. Horstemeyer, K. A. Gall, K. Dolan, J. Haskins, A.M. Gokhale, and M.D. Dighe, "Numerical, experimental, and image analyses of damage progression in cast A356 aluminum notch tensile bars," Theoretical and Applied Fracture Mechanics. Vol. 39, PP 23-45, 2003.

[12] H. Agarwal, A.M. Gokhale, S. Graham, and M. F. Horstemeyer, “Quantitative characterization of three-dimensional damage evolution in a wrought Al-alloy under tension and compression,” Metallurgical and Materials Transactions, Vol. 33A, PP. 2599-2606, 2002.

[13] H. Agarwal, A.M. Gokhale, S. Graham, and M. F. Horstemeyer, “Anisotropy of intermetallic particle cracking damage evolution in an Al-Si-Mg base wrought aluminum alloy under uniaxial compression,” Metallurgical and Materials Transactions-A, Vol. 33A, PP. 3443-3448, 2002.

[14] A. K. Balasundaram, A.M. Gokhale, S. Graham, and M. F. Horstemeyer, “Three dimensional particle cracking damage development in an Al-Mg base alloy,” Materials Science and Engineering, Vol. 355 (issue 1-2), PP. 368-383, 2003.

[15] Axio-Vision Manual, Carl Zeiss Inc.

[16] Y. Mao, A.M. Gokhale, and J. Harris, “Particle cracking damage nucleation in wrought aluminum alloys,” TMS Letters, Issue 2, PP 37-39, 2005 (On-line).

[17] A. Tewari, A.M. Gokhale, J. E. Spowart, and D. B. Miracle, “Quantitative characterization of spatial clustering in three-dimensional microstructures using two-point correlation functions,” Acta Materialia, Vol. 52, Number 2, PP. 307-319, 2004.

[18] Y. Mao, A.M. Gokhale, and J. Harris, “Computer simulations of realistic microstructures of coarse constituent particles in a hot-rolled aluminum alloy,” Computational Materials Science, Submitted (October, 2005).

[19] Alcoa, “Understanding cold finished aluminum alloys,” http://www.alcoa.com/adip/catalog/pdf/Cold_Finished_Alloy_7075.pdf. (Accessed 11/18/2005)

[20] O N Senkov, R B Bhat, S V Senkova, J D Scholz, "Microstructure and properties of cast ingots of Al-Zn-Mg-Cu alloys modified by Sc and Zr.," Metallurgical and Materials Transactions. Aug 2005. 36A, 8.

[21] W. Smith, Structure and Properties of Engineering Alloys. 2nd edition. McGraw-Hill, Inc. 1993.

[22] I.J. Polmear, Light Alloys: Metallurgry of the Light Metals, 3rd edition. Halsted Press. 1996.

[23] R. Ayer, J.Y. Koo, J.W. Steeds, B.K. Park, Metall. Trans. A 16A, 1985. p 1925.

[24] M. Gao, C.R. Feng, R.P. Wei, Metall. "An analytical electron microscopy study of constituent particles in commercial 7075-T6 and 2024-T3," Alloys Mater. Trans. A 29. 1998. pg 1145.

[25] F. Andreatta, H. Terryn, J.H.W. de Wit, "Corrosion behaviour of different tempers of AA7075 aluminium alloy," Electrochimica Acta 49 (2004) 2851-2862.

[26] A.S. Argon, J. Im, and R. Safoglu, Metall. Trans. A., 1975, vol 6a, p. 825-837.

[27] K. Tanaka, T. Mori, and T. Nakamura, Phil. Mag., 1970, vol. 21, p. 267.

[28] D. Broek: "A study on ductile fracture," PH.D. Thesis, Delft, Netherlands, 1971.

[29] M. F. Ashby, Phil. Mag., 1966, vol. 14, p. 1157.

[30] F.A. McClintock, Ductility, p. 255, ASM, Metals Park, Ohio, 1968.

[31] C. Zener, "Fracturing of metals," ASM, Metals Park, Ohio, 1949, p. 3.

[32] J. Yeh and W. Liu, Metall and Mat. Trans. 1996, vol 27a, p. 3558-3569.

[33] A.N. Stroh, Adv. Phys., 1957, vol. 6, pp. 418-65.

[34] N.J. Petch, “Toughness and brittleness of metals,” Institution of Metallurgists, Interscience Publishers Inc., New York, NY, 1961.

[35] E. Smith and J.J. Barnby, Met. Sci. J.,1967, vol. 1, p. 56.

[36] T.C. Lindley, G. Oates, and C.E. Richards, Acta Metall., 1970 vol. 18, pp. 1127-36.

[37] T.B. Cox and J.R. Low, Jr., Metall. Trans., 1974, vol. 5, pp. 145-70.

[38] A.S. Argon, J. Im, and R. Safoglu, Metall. Trans. A, 1975, vol. 6A, pp. 825-37.

[39] L.M. Brown and W.M. Stobbs, Phil. Mag., 1976, vol 34, pp. 351-72.

[40] R. Doglione, J.L. Douziech, C. Berdin, D. Francois, “Microstructure and damage mechanisms in A356 alloy,” Material Science Forum, 1996, pp. 130-139.

[41] F.A. McClintock, “Ductility,” ASM, Metals Park, Ohio, 1968, pp. 255-275.

[42] C. Zener, “The micro-mechanism of fracture,” Fracturing of Metals, ASM, Metals Park, Ohio, 1948.

[43] K. Tanaka, T. Mori, T. Nakamura, “Cavity formation at the interface of a spherical inclusion in a plastically deformed matrix,” Phil. Mag, 1967, vol. 21.

[44] J. Gurland, Acta Metall., 1972, vol. 20, pp. 735-41.

[45] B.I. Edelson and W.M. Baldwin, Jr., Trans. ASM, 1962, vol. 55, pp. 230-50.

[46] Gokhale, “Quantitative characterization and representation of global microstructural geometry,” ASM Handbook, Vol 9. p 428-445.

[47] H.J.G. Gundersen, “Note on estimation of number density of arbitrary profiles: the edge effect,” J. Microsc., Vol 11, 1977, p 219-223.

[48] H. Argawal, M.S. Thesis Dissertation, Georgia Institute of Technology, 2001.

[49] A. Tewari, A.M. Gokhale, J.E. Spowart, and D.B. Miracle, “Quantitative characterization of spatial clustering in three-dimensional microstructures using two-point correlation functions,” Acta Mater., Vol. 52, 2004, p307-319.

[50] D.C. Sterio, “ The unbiased estimation of number and size of arbitrary particles using disector,” Journal Microscopy. 134 ,1984, p127.

[51] A. Tweari, A.M. Gokhale, Journal Microscopy. 200, 2000, p227.

[52] A. Tewari, A.M. Gokhale, R.M. German, “Effect of gravity in three-dimensional coordination number distribution in liquid phase sintered microstructures,” Acta Mater. 47, 1999, p3721.

[53] Rhines FN, Craig KR, “Measurement of average grain volume and topological parameters by serial sectioning analysis,” Metal Trans, A 1976, 7A, p1729-34.

[54] Spowart JE, Mullens HM, Puchala BT, “Collecting and analyzing microstructures in 3 dimensions: a fully automated approach,” J Met, 2003, Oct., p35-7.

[55] Harpreet Singh, AM Gokhale, “Visualization of three dimensional microstructures,” Mater Char. 54, 2005, p21-29.

[56] Y. Mao, A.M. Gokhale, and J. Harris, “Computer simulations of realistic microstructures of coarse constituent particles in a hot-rolled aluminum alloy,” Journal of Microscopy, (submitted)

[57] Singh H, Gokhale AM, Mao Y and Spowart JE, “ Computer simulations of realistic microstructures of discontinuously reinforced aluminum (DRA) composites,” Acta Materialia (submitted)

[58] Singh H, Mao Y and Gokhale AM, “Application of digital image processing for implementation of complex realistic particle shapes/morphologies in computer simulated heterogeneous microstructures,” Modeling and Simulation in Materials Science and Engineering (submitted)

[59] ASM Metals Handbook, “Specific metals and alloys.”

[60] C.H. Caceres and J.R. Griffiths, “Damage by the cracking of silicon particles in an Al-7Si-.4Mg casting alloy,” Acta Mater. Vol 44, No. 1, 1996, pp 25-33.

[61] Y. Brechet, J.D. Embury, S. Tao, and L. Luo, “Damage initiation in metal matrix composites,” Acta Matall. Mater. Vol. 39, No. 8, 1991, pp. 1781-86.